Q19960122000 8

3/10

MECHANICAL ANALYSES OF A YUCCA MOUNTAIN FAULT MODEL

Goodluck I. Ofoegbu and David A. Ferrill
Center for Nuclear Waste Regulatory Analyses
Southwest Research Institute
San Antonio, Texas 78238-5166
(210)522-6641 and 6082

ABSTRACT

Hangingwall deformations associated with listric faulting are analyzed using finite element modeling. Results of parametric investigations show that hangingwall response is strongly sensitive to *in situ* stress and that ground accelerations induced by fault slip are sensitive to the damping response of fault-zone materials. Other factors that have strong effects on hangingwall deformation associated with listric faulting include subsurface fault geometry (i.e., continuous listric shape versus steeply dipping fault terminating abruptly at a deep-seated detachment) and fault zone rheology (i.e., thin zone of weak isotropic solid versus block-on-block contact).

I. INTRODUCTION

The Nuclear Regulatory Commission (NRC) is required to review a license application from the U.S. Department of Energy to construct and operate a proposed repository for high-level radioactive waste at Yucca Mountain (YM), Nevada. YM lies in a tectonically active area, containing numerous normal faults. Key issues to be considered in the evaluation of the anticipated application include whether a mined geologic repository at that location will provide effective long-term waste isolation from the accessible environment and whether short-term safety and retrievability objectives will be met as specified in 10 CFR Part 60. Because of risks to long-term performance associated with structural (geologic) deformation and seismicity, potentially adverse conditions related to structural deformation and seismicity have been included in 10 CFR Part 60: (i) structural deformation such as uplift, subsidence, folding, or faulting that may adversely affect the regional groundwater flow system [60.122(c)(4)]; (ii) structural deformation such as uplift, subsidence, folding, and faulting that may have occurred during the Quaternary Period (i.e., within the last approximately 2 million yr) [60.122(c)(11)]; (iii) earthquakes that have occurred historically that, if they were to be repeated, could affect the site significantly [60.122(c)(12)]; (iv) indications, based on correlations of earthquakes with tectonic processes and features, that may increase either the frequency of occurrence or the magnitude of earthquakes [60.122(c)(13)]; (v) more frequent occurrence of earthquakes or earthquakes of higher magnitude than are typical of the area in which the geologic setting is located [60.122(c)(14)]. In addition, design criteria must be met to provide protection against natural phenomena as also specified in 10 CFR Part 60: the structures, systems, and components important to safety shall be designed so that natural phenomena and environmental conditions anticipated at the geologic repository operations area will not interfere with necessary safety functions [60.131(b)(1)]. Because of these regulatory concerns regarding structural deformation and seismicity, it is critical that the geologic structure of YM is well understood, including the potential for displacement and seismicity on the existing faults.

There is considerable uncertainty regarding the subsurface fault geometry beneath YM and Crater Flat Valley.[1] Fig. 1 shows two alternative models of the subsurface fault geometry, one based on the interpretation of the YM faults as part of a west-dipping listric system with a detachment at a depth of 6–7 km (i.e., well within the brittle crust),[1, 2, 3] and the other based on the interpretation that the YM faults extend steeply to the base of the Bare Mountain Fault at a depth of about 10–12 km (i.e., in the brittle-ductile transition zone).[4]

Normal faults that have listric shapes or are concave-upward in profile are a common feature in extensional tectonic regions. Because of the fault shape,

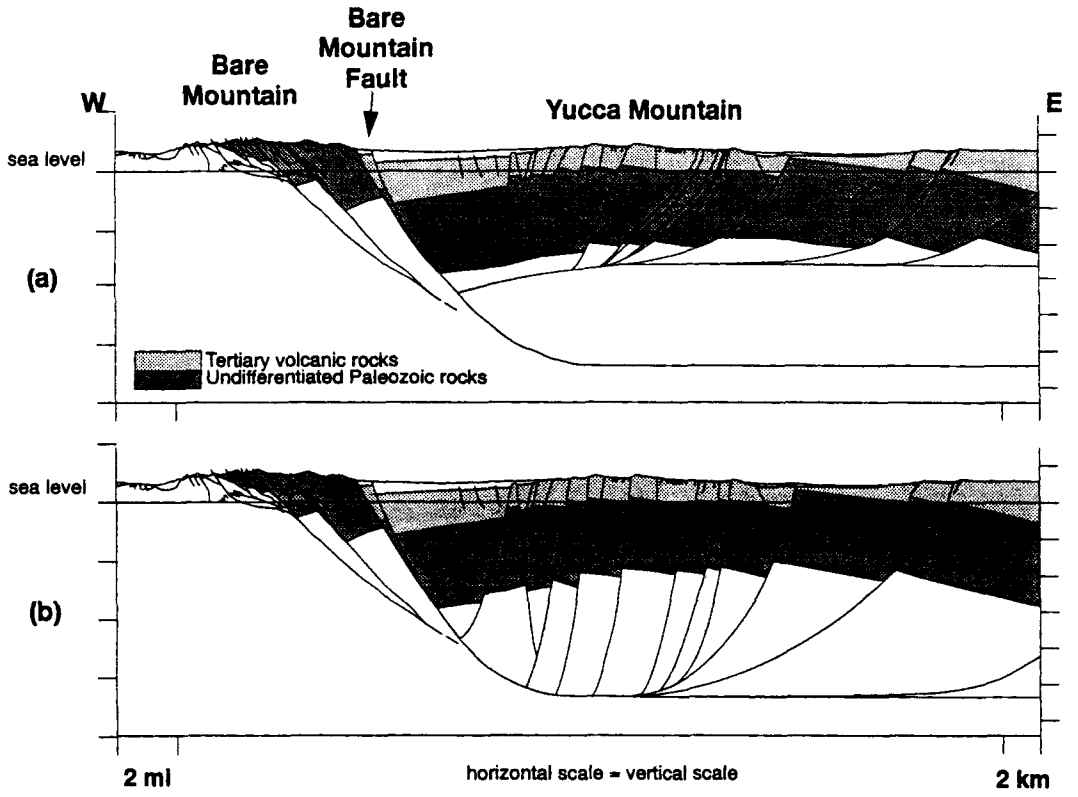

Figure 1: Geologic cross section along an approximately east-west path through the proposed repository site based on two alternative models of the subsurface fault geometry

extension parallel to the low-angle part of a listric normal fault necessitates deformation of the hangingwall, footwall, or both, leading to features such as hangingwall rollover folds[5, 6] and footwall uplift.

The mechanical argument against listric normal faulting is that, in regions of extensional faulting, the normal stress on a subhorizontal fault would be nearly equal to the maximum principal compressive stress. As a result, the occurrence of slip on such faults cannot be explained in terms of the Mohr-Coulomb strength criterion.[7, 8]

Another argument against listric normal faulting arises from the fact that evidence for seismic slip on low-angle normal faults is extremely rare.[9, 10] The vast majority of earthquakes related to normal faulting occur in the depth range of 6 to 15 km on 30°–60° dipping faults.[11] On the other hand, it has been suggested that the lack of seismicity on low-angle faults does not reflect lack of slip on the faults but instead that slip on such faults probably occurs at aseismic rates (considering the classification proposed by Beroza and Jordan,[12] for comparison) and may either precede or postdate seismic slip on high-angle portions of the fault.[13]

In the current study, two-dimensional finite element analyses are performed on a cross section similar to the upper-crustal YM fault system modeled in Fig. 1(a). These analyses evaluate the effects of subsurface fault geometry on predictions of ground-surface deformations, fault displacement, ground accelerations associated with fault slip, and interactions among the various faults. A basic question examined in the analyses is whether slip on one of the faults that belong to a listric fault system could trigger slip on the other faults within the system. In addition, the effects of *in situ* stress and material properties on the predicted response are examined through parametric analyses.

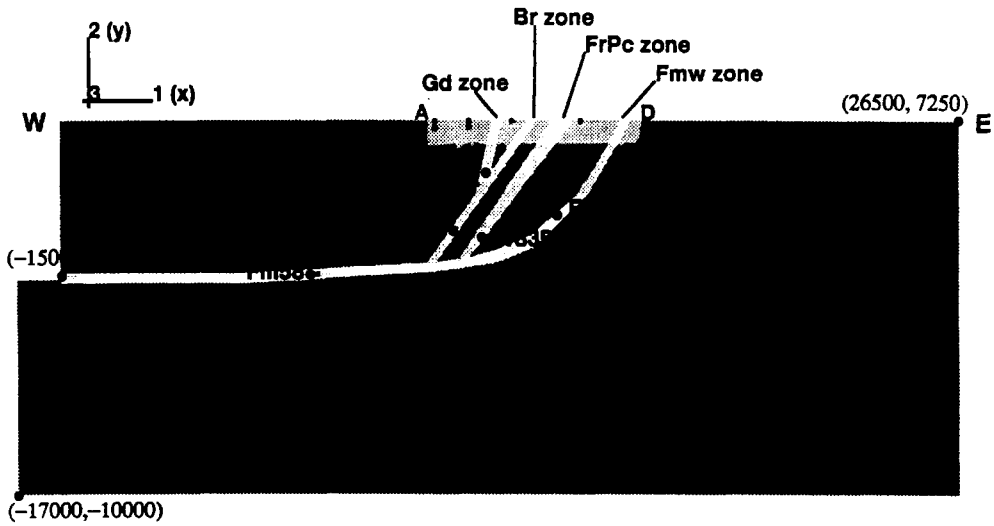

Figure 2: Geometrical model showing boundaries, fault zones, and stations monitored for slip rate and ground accelerations. All dimensions are in meters.

II. DESCRIPTION OF MODEL

Fig. 2 shows the geometrical model used for the finite element analyses. The modeled faults are referred to as the Gd, Br, FrPc, and Fmw fault zones, which are similar in attitude to the Ghost Dance Fault, Bow Ridge Fault, Fran Ridge and Paintbrush Canyon fault system, and the interpreted Fortymile Wash Fault, respectively, based on the structural-geologic cross section presented in Fig. 1(a). Each fault was represented as a 500-m thick zone of solid material that was assigned material properties different from those of the surrounding rock, as is explained later. The choice of thickness for the fault zones was influenced by meshing considerations but may also be justified considering the field evidence[3] that the faults that are of interest in the study consist of zones of breccia and densely fractured rock up to 1 km wide on the ground surface.

The rate of fault slip was monitored at five stations shown in Fig. 2 as Fm58, Fm168, Fr635, Br833, and Gd3194. Stress changes induced by fault slip were monitored in the region bounded by ABCD. The stress-change study zone covers a horizontal distance of about 10 km and extends vertically to a depth of about 1 km from the ground surface. The interest in such a zone arises from the anticipated location of the proposed repository at a depth of about 300 m below the ground surface. The six dark dots within the stress-change study zone indicate stations at which ground acceleration was monitored. The acceleration stations are located within the epicentral zones of slip events that may originate near the base of the steeply dipping faults.

A. Material Model

The fault-zone materials were modeled as elastoplastic with an isotropic yield strength. The rest of the rock mass (the footwall of the Fmw zone and the part of the hangingwall outside the fault zones) was modeled as linear-elastic with a constant Young's modulus $E = 32.5$ GPa and Poisson's ratio $\nu = 1/3$. The same values of E and ν were also applied to the elastoplastic material zones. The strength and flow properties for the elastoplastic zones were defined in terms of the unconfined compressive strength q_u, friction angle ϕ, and the dilation angle φ. The fault zones are expected to be essentially cohesionless; therefore, q_u was assigned a relatively small constant value of 1.0 MPa. The values of ϕ were varied in the range $30° \leq \phi \leq 40°$ and those of the ratio φ/ϕ were varied in the range $0 \leq \varphi/\phi \leq 1$. The damping response (i.e., absorption of dynamic energy due to inelastic deformation) of the elastoplastic zones was defined in terms of the damping factor D_α, the values of which were varied in the $0.01 \leq D_\alpha \leq 0.1$ range.[14]

B. Initial and Boundary Conditions

The medium was assumed to be under zero strain at the initial state, because strains associated with previ-

ous deformations are not relevant to the investigation, except to the extent that they may assist in defining the initial stress state. The maximum principal compressive stress, σ_1, was assumed to be vertical and its magnitude was computed using a vertical gradient of 25 MPa/km. Possible effects of vertical density variations on the vertical stress gradient were ignored, because it is believed that uncertainties related to the ratios of the principal stresses are likely to be more important than those related to the absolute magnitude of the vertical principal stress.

Considering that the Yucca Mountain area falls within the Basin and Range extensional tectonic region,[8] the minimum principal compressive stress, σ_3, is believed to be horizontal and nearly normal to the strike of the fault planes. Under such conditions, values of the ratio σ_3/σ_1 (denoted k_3) would lie in the range $k_a \leq k_3 \leq k_o$, where k_a is the value of the ratio for the condition of incipient failure under pure horizontal extension, and k_o is its value under the state of zero horizontal deformation, often referred to as the at-rest or uniaxial strain state.[15] Therefore the values of k_3 were varied in the range $0.2 \leq k_3 \leq 0.5$. Such assumed values of k_3 are not intended to represent the actual values for the Yucca Mountain area, but are used in investigations that may help determine the extent to which predictions made for Yucca Mountain may be sensitive to the value of the k_3 parameter.

The magnitude of the intermediate principal stress, σ_2, for the region is believed to be closer to that of the maximum principal stress than to the minimum.[16, 17] Moreover, the intermediate principal stress has little influence in a two-dimensional analysis for which the maximum and minimum principal stresses lie in the plane of the analysis. As a result, the intermediate principal stress was assigned an initial-state value of $0.9\sigma_1$.

The boundary conditions are (Fig. 2): free-surface conditions at the top of the model; zero vertical displacement at the base, and zero horizontal displacement at the left and right boundaries, of the footwall; vertical downward pressure of 183.33 MPa on the left-end horizontal bench; and horizontal pressure of $0.025k_3d$ MPa (where d is the depth in meters) on the part of the left boundary above the bench. The distance of the base and vertical boundaries of the model from the fault zones was set long enough to increase the travel time for energy reflected at the boundaries, thereby preventing such reflected energy from influencing the calculated response.

C. Simulation Procedure and Numerical Experiment Design

Each simulation was conducted in two steps. First, the initial equilibrium state was established through static analysis, considering the initial stress, gravitational forces, and the boundary conditions. Thereafter slip was induced on a selected fault zone in a dynamic-analysis step, through an instantaneous reduction of the friction angle for the fault to the value required to satisfy the Mohr-Coulomb condition for incipient slip. The selected response variables were monitored for a period of 5 seconds, which was long enough to allow adequate recording of the response history but short enough to ensure that the calculated response is not influenced by energy reflected from the boundaries.

The friction-angle reduction was applied to one fault at a time. The perturbed faults are: (1) the upper (steep) segment of the Fmw fault zone, (2) the FrPc fault zone, (3) the Br fault zone, and (4) the entire Fmw fault zone. The response of the medium to such fault perturbations was expected to vary, depending on the values assigned to the input parameters k_3, ϕ, φ/ϕ, and D_α. Therefore, the numerical experiment consisted of monitoring the response of the medium to fault slip under several combinations of the four input parameters and the perturbed fault. The response was monitored in terms of fault displacement, slip rate, slip length, limit-equilibrium friction angle (i.e., the smallest friction angle that would prevent slip on a fault), maximum vertical and horizontal ground accelerations, and the area of the zone of potential instability within the stress-change study zone (considering the occurrence of slip on planes dipping 65°, 75°, or 80°, with the values of friction angle for such planes set to 30° and 40°).

The input-parameter combinations were generated in terms of the normalized values of k_3, ϕ, φ/ϕ, and D_α. The normalized value, θ_r, of a given variable θ is equal to the ratio $(\theta - \theta_{\min})/(\theta_{\max} - \theta_{\min})$, where $\theta_{\max}$ and $\theta_{\min}$ are the maximum and minimum values, respectively, of θ. A set of 17 combinations of values of four θ_r-type variables were generated randomly and converted to values of k_3, ϕ, φ/ϕ, and D_α, and each combination was applied to the perturbation of each fault, giving a total of 68 simulations.

III. ANALYSES OF CALCULATED RESULTS

Figures 3, 4, and 5 show typical calculated responses associated with slip on the Fmw fault zone. The figures represent the condition at the end of 5 s

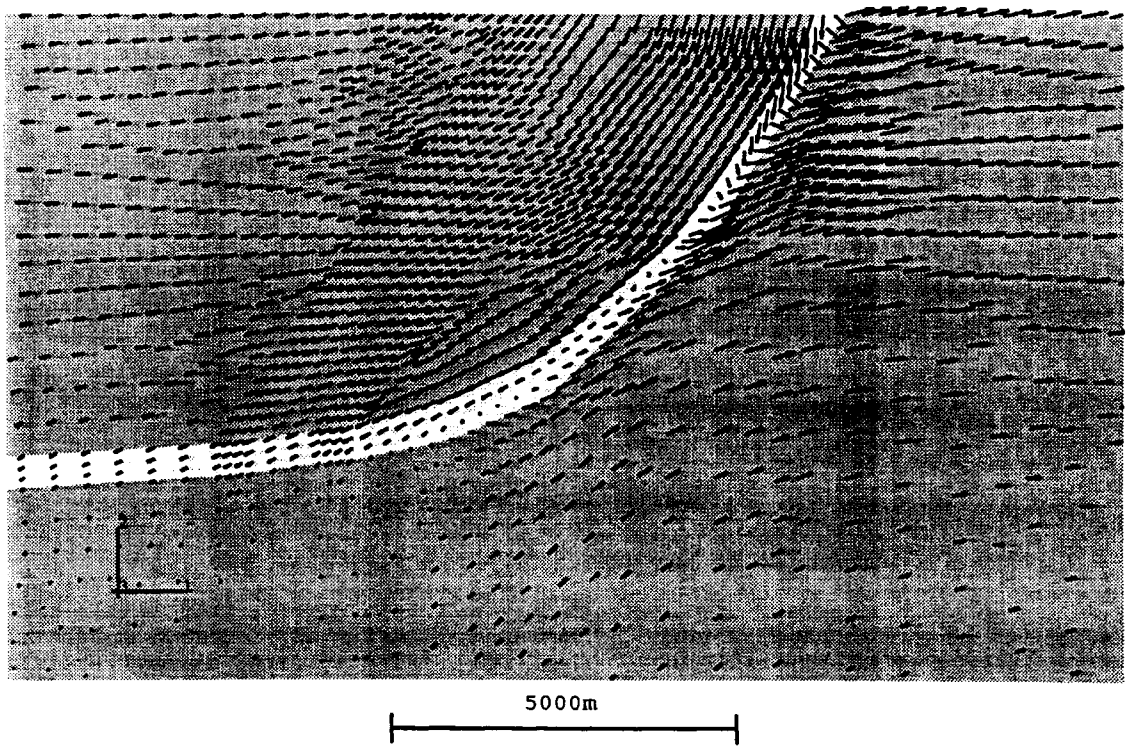

Figure 3: Distribution of displacement vectors associated with slip on the Fmw fault zone. Arrow lengths normalized with respect to maximum displacement of 1.018 m.

following the perturbation of the Fmw fault with the input-parameter values $k_3 = 0.4$, $\phi = 30°$, $\varphi/\phi = 0.1$, and $D_\alpha = 0.05$. The figures illustrate the following features of the calculated responses:

(1) The calculated displacement pattern consists of upward-eastward displacements on the footwall and downward-westward displacements on the hangingwall. Also, the ground-surface profile includes footwall uplift and hangingwall rollover that decrease in magnitude away from the fault. These features of the calculated displacements agree well with features usually associated with slip on listric normal faults.[5]

(2) The displacement vectors in the low-angle detachment are generally inclined to the fault, have a downward-westward sense, and are large relative to those in neighboring areas of the footwall. Such a distribution of displacement vectors is consistent with the occurrence of oblique shear zones referred to as Riedel shears[18, 19] within the low-angle detachment. This observation regarding possible occurrence of Riedel shears in the low-angle detachment suggests that oblique slip planes should also be considered in assessing the potential for slip within such fault zones. As a result, it is likely that an isotropic strength criterion, such as was applied in this study, would simulate the mechanical behavior of low-angle detachment faults that lie within the brittle crust more correctly than would a strength criterion that restricts the development of inelastic response to fault-parallel planes.

(3) As Fig. 5 shows, the magnitude of plastic strain is largest in the steep segments and smallest in the low-angle segments of the listric fault. Typically, slip initiated near the base of the steep segment and propagated upward toward the ground surface and downward toward the detachment. Such a pattern of slip propagation is consistent with the initiation of seismic events deep within the crust and upward propagation of the associated faults toward the ground surface. An examination of the range of values of the calculated slip rates[20] shows the following: (i) The rates of induced slip (i.e., slip on a fault caused by a perturbation of the same fault as defined earlier) are generally about three orders of magnitude larger than the rates of triggered slip (i.e., slip on a fault caused by the induced slip on another fault). (ii) The rates of induced slip on the

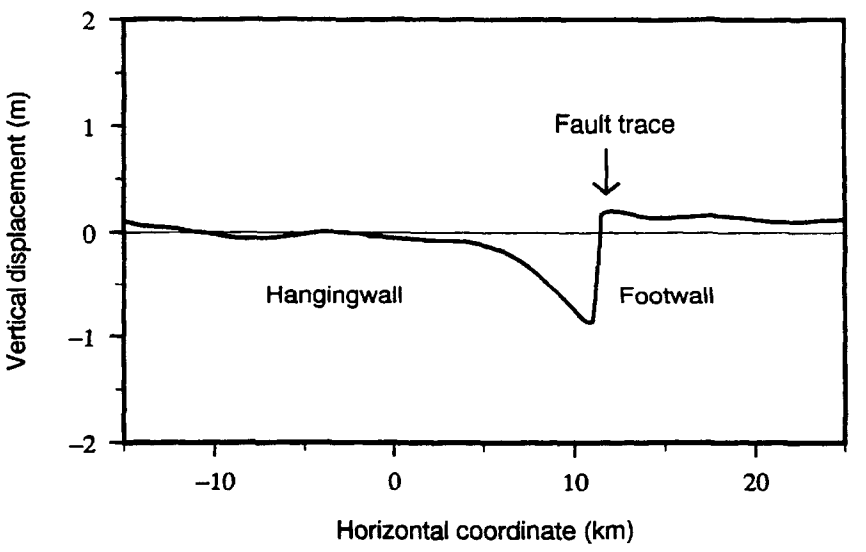

Figure 4: Ground-surface profile associated with slip on the Fmw fault zone

low-angle detachment are up to two orders of magnitude smaller than the rates of induced slip on the steep segments of the same fault. (iii) The rates of triggered slip on the low-angle detachment associated with the perturbation of any of the steeply dipping faults (i.e., the Br, FrPc, or steep segment of Fmw fault zones) are about six orders of magnitude smaller than the rates of the induced slip. Considering the classification of lithospheric deformation rates proposed by Beroza and Jordan,[12] such variations of slip rate are interpreted to imply that the low-angle detachment fault is likely to slip aseismically in response to seismic slip events in the associated steeply dipping faults.

A. Effects of Subsurface Fault Geometry on Hangingwall Response

The geometrical model applied in the study includes two types of subsurface fault geometry; namely, broadly curved faults with dip that changes gradually from steep to low angle (represented in the study by the Fmw fault), and steeply dipping faults that terminate abruptly at a low-angle detachment (such as the FrPc and Br faults). Several aspects of the calculated hangingwall response lead to the conclusion that slip on a broadly curved fault has more severe effects on the hangingwall than slip on the planar steeply dipping faults.

First, an examination of the down-dip profiles of fault displacement[20] showed that the displacement on each fault occurred mainly in the steeply dipping segments. For the Fmw fault zone, most of the displacement occurred over only about 25 per cent of the down-dip length. On the other hand, the displacement in the FrPc and Br fault zones occurred over about 75 per cent of the down-dip length. Such nonuniform distributions of fault displacement imply significant deformations of the hangingwall and footwall that increase in severity as the nonuniformity of the fault-displacement distribution increases. As a result, hangingwall and footwall deformations associated with slip on listric faults (such as the Fmw fault) are expected to be more severe than those associated with slip on planar faults (such as the FrPc or Br faults).

Second, whereas the length of the Gd fault over which triggered slip occurred[20] in response to a perturbation of the Fmw fault attained a maximum of about 2 km, the maximum slip length on the Gd fault caused by a perturbation of either the FrPc or the Br fault was only about 0.5 km.

Third, the maximum vertical and horizontal ground accelerations induced at any of the monitored stations by a perturbation of the Fmw fault were 0.35 g and 0.39 g, respectively. On the other hand, the maximum values of induced accelerations for the FrPc or Br fault zones were 0.27 g vertically and 0.19 g horizontally.[20]

Fourth, the area of the zone of potential instability associated with slip on the Fmw fault is much larger than that associated with slip on the FrPc or Br fault. Potential instability was determined based on the slip tendency[20, 21] for planar discontinuities within

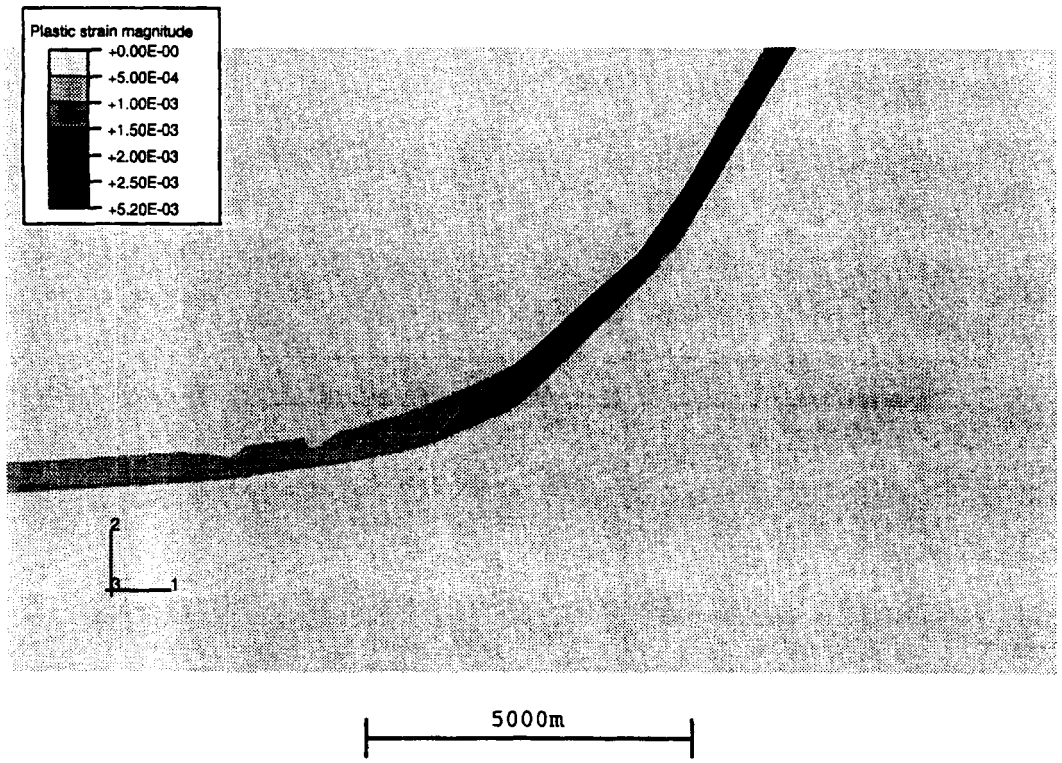

Figure 5: Distribution of plastic-strain magnitudes associated with slip on the Fmw fault zone.

the stress-change study zone that dip westward at 65°, 75°, or 80°.

B. Sensitivity of Response Variables to Input Parameters

A sensitivity analysis of the calculated responses was conducted to identify the input parameters that have dominant effects on the response variables. The analysis was based on scatter plots of the response variables versus the input parameters, both normalized in the manner defined for the ratio θ_r. Such plots were used to determine whether there was significant correlation between pairs of response and input variables, based on visual examination only. For example, Figs. 6 and 7 show the sensitivity of the fault displacement in the Fmw fault zone, $D_{f(\mathrm{Fmw})}$, to changes in the values of k_3 and ϕ, respectively. As the two figures show, whereas significant correlation occurs between $D_{f(\mathrm{Fmw})}$ and k_3, there is no discernable correlation between $D_{f(\mathrm{Fmw})}$ and ϕ.

A significant correlation between a pair of response variable and input parameter implies that the variability of the particular input parameter has a dominant effect on the predicted values of the response variable. On the other hand, the absence of significant correlation implies that any effect of the variability of the input parameter on the response variable is overshadowed by the variability of other input parameters. This distinction between input parameters that have a dominant effect and those that do not leads to recommendations regarding the input parameters that can be assigned single values and those whose values need to be varied within a range, in an analysis to predict values of a selected response variable. For example, the results presented in Figs. 6 and 7 imply that the parameter ϕ may be assigned a single value whereas k_3 needs to be varied to examine its effect in an analysis to evaluate the response variable $D_{f(\mathrm{Fmw})}$.

The results of the sensitivity analysis[20] lead to the following conclusions: (1) The variability of the *in situ* stress ratio k_3 has a dominant effect on the predicted hangingwall response, except the magnitudes of ground acceleration. (2) The variability of the damping factor D_α has a dominant effect on the predicted ground accelerations within the hangingwall. (3) The effects

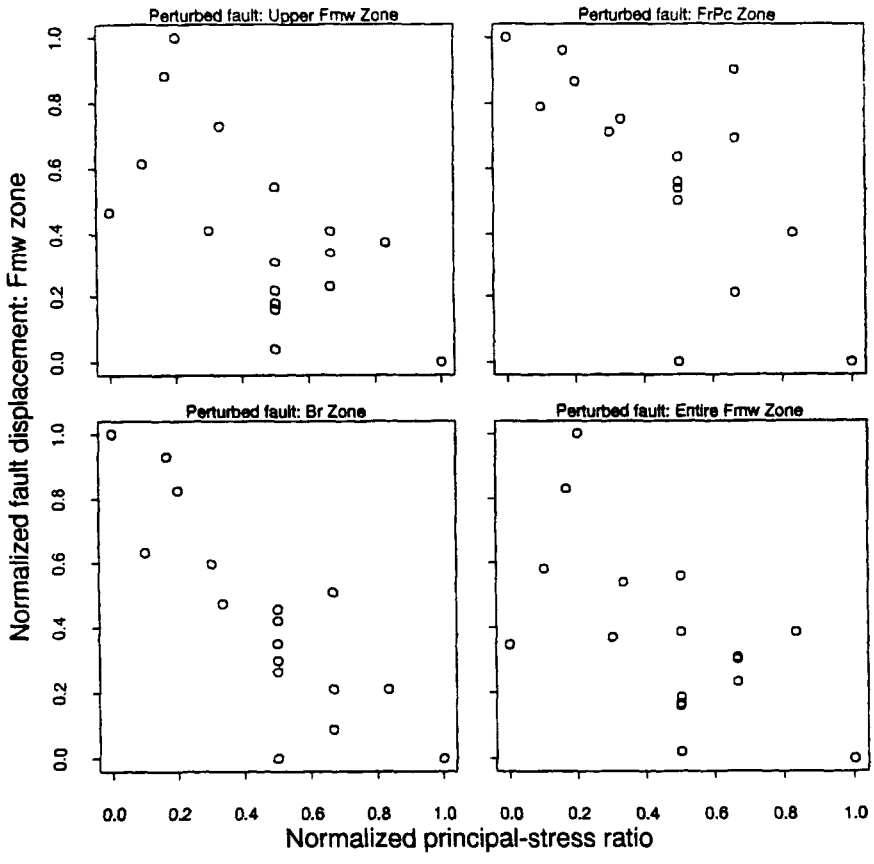

Figure 6: Sensitivity of Fmw fault displacement to changes in the value of the principal stress ratio k_3

of the variabilities of ϕ, φ/ϕ, and D_α on all aspects of hangingwall response except ground accelerations are overshadowed by the effects of the variability of k_3. (4) The effects of the variabilities of k_3, ϕ, and φ/ϕ on ground accelerations are overshadowed by the effects of the variability of D_α. Therefore, in an analysis to predict the values of ground acceleration, each of the parameters k_3, ϕ, and φ/ϕ may be assigned a single value whereas the effects of varying D_α should be examined. For analyses to predict other aspects of hangingwall response, the effects of the variability of k_3 should be examined, but the parameters ϕ, φ/ϕ, and D_α may each be assigned a single value.

CONCLUSIONS

1. The values of *in situ* stress used in the analyses of hangingwall deformations deserve particular attention. For such analyses, *in situ* stress data are required, preferably based on measurements at depths below the zone of influence of ground-surface topography, in order to define the range of values of the initial principal stress ratios.

2. For analyses to predict the values of ground acceleration, it is necessary to constrain damping as much as possible, and then to evaluate the range of accelerations for the range of accepted values of the material damping factor.

3. Slip on a broadly curved fault that changes dip gradually from steep to low-angle has greater impact on hangingwall deformation than slip on steeply dipping faults that terminate abruptly at a low-angle detachment. For example, slip on the interpreted Fortymile Wash Fault produced greater impact on hangingwall deformation than did slip on the other faults.

4. Slip rates in the low-angle segments of the modeled listric fault system were found to be several orders of magnitude smaller than the associated slip rates in the steep segments. Such differences in slip rate may explain the lack of seismicity associated with low-angle faults. Slip on low-angle

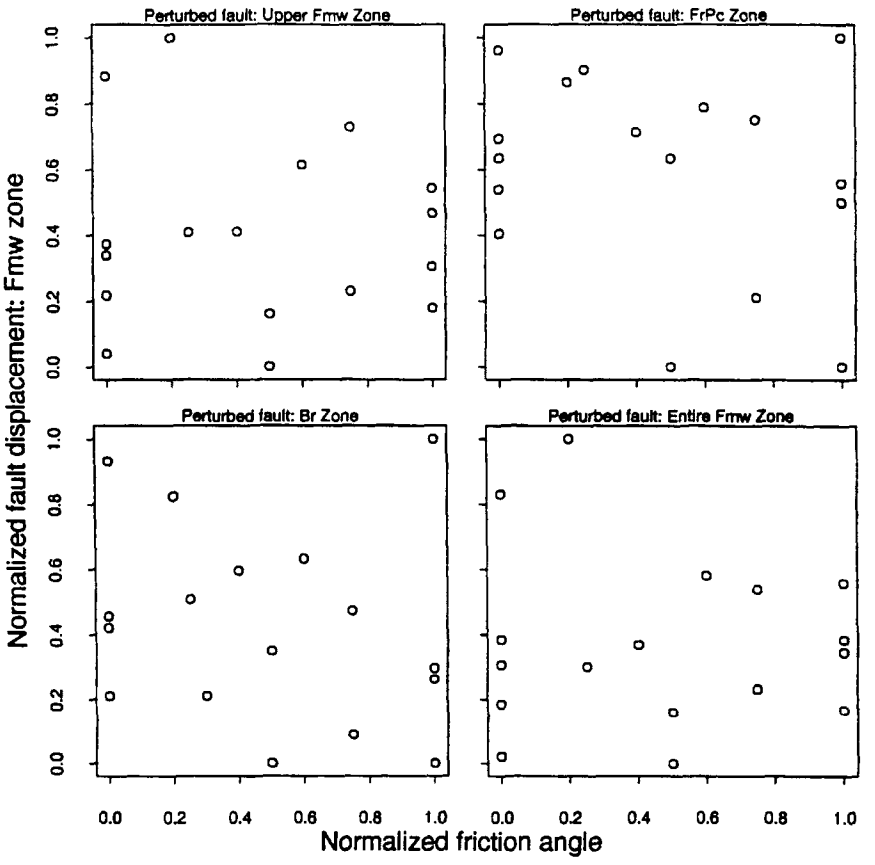

Figure 7: Sensitivity of Fmw fault displacement to changes in the value of the friction angle ϕ

faults may occur at aseismic rates and either precede or postdate seismic slip on high-angle fault segments.

5. The best approach to modeling listric faults contained entirely in the brittle crust is to represent each fault as a thin, relatively weak zone with isotropic properties.

ACKNOWLEDGEMENTS

The work described in this paper was performed at the Center for Nuclear Waste Regulatory Analyses (Southwest Research Institute, San Antonio, Texas) for the NRC under contract number NRC-02-93-005. The work was done on behalf of the NRC Office of Nuclear Material Safety and Safeguards, Division of Waste Management. The views expressed in the paper are those of the authors and do not necessarily reflect the views or regulatory position of the NRC.

The authors are grateful to S. Young, R. Hofmann, A.P. Morris, and H.L. McKague for technical contributions made at various stages of the project. The finite element analyses described in this paper were conducted using ABAQUS.[22]

REFERENCES

1. S. R. Young, G. L. Stirewalt, and A. P. Morris, Geometric Models of Faulting at Yucca Mountain, Technical Report CNWRA 92-008, Center for Nuclear Waste Regulatory Analyses, San Antonio, Texas (1992).

2. R. B. Scott and J. Bonk, Preliminary Geologic Map of Yucca Mountain, Nye County, Nevada, with Geologic Sections, 1:12000, Technical Report USGS-OFR-84-494, U. S. Geological Survey (1984).

3. R. B. Scott, "Tectonic Setting of Yucca Mountain, Southwestern Nevada," *Basin and Range Extensional Tectonics Near the Latitude of Las*

Vegas, Nevada, B. P. Wernicke, ed., *Geol Soc Am Mem*, **176**, pp. 251–282 (1990).

4. T. D. Gilmore, Geodetic Leveling Data Used to Define Historical Height Changes Between Tonopah Junction and Las Vegas, Nevada, Technical Report USGS-OFR-92-450, U. S. Geological Survey (1992).

5. W. K. Hamblin, Origin of "reverse drag" on the downthrown side of normal faults, *Geol Soc Am Bull*, **76**, pp. 1145–1164 (1965).

6. W. F. Dula, Jr., Geometric models of listric normal faults and rollover folds, *Am Assoc Pet Geol Bull*, **75**, pp. 1609–1625 (1991).

7. R. H. Sibson, A note on fault reactivation, *J Struct Geol*, **7**, pp. 751–754 (1985).

8. D. A. Ferrill, A. P. Morris, D. B. Henderson, and R. H. Martin, "Tectonic processes in the central Basin and Range region," *NRC High-Level Radioactive Waste Research at CNWRA, July-December 1994*, B. Sagar, ed., pp. 121–139, Center for Nuclear Waste Regulatory Analyses, San Antonio, Texas (1995).

9. G. A. Abers, Possible seismogenic shallow-dipping normal faults in the Woodlark-D'Entrecasteaux extension province, Papua New Guinea, *Geology*, **19**, pp. 1205–1208 (1991).

10. R. A. Johnson and K. L. Loy, Seismic reflection evidence for seismogenic low-angle faulting in southeastern Arizona, *Geology*, **20**, pp. 597–600 (1992).

11. J. A. Jackson, "Active normal faulting and crustal extension," *Continental Extensional Tectonics*, M. P. Coward et al., eds., *Spec Publ Geol Soc London*, **28**, pp. 3–17 (1987).

12. G. C. Beroza and T. H. Jordan, Searching for slow and silent earthquakes using free oscillations, *J Geophys Res*, **95**(B3), pp. 2485–2510 (1990).

13. H. J. Melosh, Mechanical basis for low-angle normal faulting in the Basin and Range Province, *Nature*, **343**, pp. 331–335 (1990).

14. F. E. Richart, R. D. Woods, and J. R. Hall, *Vibrations of Soils and Foundations*, Prentice-Hall, Englewood Cliffs, New Jersey (1970).

15. J. C. Jaeger and N. G. W. Cook, *Fundamentals of Rock Mechanics*, Chapman and Hall, London, third edition (1979).

16. S. C. Harmsen, The Little Skull Mountain, Nevada, earthquake of 29 June 1992: Aftershock focal mechanisms and tectonic stress field implications, *Bull Seism Soc Am*, **84**(5), pp. 1484–1505 (1994).

17. J. M. Stock, J. H. Healy, S. H. Hickman, and M. D. Zoback, Hydraulic fracturing stress measurements at Yucca Mountain, Nevada, and relationship to regional stress field, *J Geophys Res*, **90**(B10), pp. 8691–8706 (1985).

18. A. W. Skempton, Some observations on tectonic shear zones, *Int Soc Rock Mech Congr Proc*, **1**, pp. 329–335 (1966).

19. R. H. Groshong, Jr., Low-temperature deformation mechanisms and their interpretation, *Geol Soc Am Bull*, **100**, pp. 1329–1360 (1988).

20. G. I. Ofoegbu and D. A. Ferrill, Finite Element Modeling of Listric Normal Faulting, Technical Report CNWRA 95-008, Center for Nuclear Waste Regulatory Analyses, San Antonio, Texas (1995).

21. D. A. Ferrill, G. L. Stirewalt, D. B. Henderson, J. A. Stamatakos, A. P. Morris, B. P. Wernicke, and K. Spivey, Faulting in the Yucca Mountain Region: Critical Review and Analyses of Tectonic Data From the Central Basin and Range, Technical Report CNWRA 95-017, Center for Nuclear Waste Regulatory Analyses, San Antonio, Texas (1995).

22. Hibbit, Karlsson and Sorensen, Inc., *ABAQUS Users' Manual, Version 5.4*, Pawtucket, Rhode Island (1994).

13/10

Finite Element Modeling of Listric Normal Faulting[1]

G.I. Ofoegbu and D.A. Ferrill
Center for Nuclear Waste Regulatory Analyses
Southwest Research Institute
San Antonio, Texas 78238-5166
USA
Phone: (210)–522–6641 and 6082

[1]Prepared for the *Int. J. Rock Mech. Min. Sci. & Geomech. Abstr.*, August 1995

Abstract

The results of finite element analyses of hangingwall deformation associated with listric faulting are presented in this paper. Hangingwall deformation is demonstrated to be strongly sensitive to the values of *in situ* stress. In addition, the magnitudes of ground acceleration induced in the hangingwall by slip on listric faults are sensitive to the amount of material damping in the fault zones. On the other hand, the sensitivity of hangingwall deformation to material parameters such as friction and dilation angles, damping factor, and elastic stiffness is overshadowed by the *in situ* stress effects.

The results also indicate a strong effect of fault geometry on hangingwall deformation. Faults that gradually change in attitude from steeply to gently dipping cause more severe effects on the hangingwall than planar steeply dipping faults that terminate abruptly at a low-angle detachment. It was also observed that slip on the low-angle segment of a listric fault system occurs at a rate several orders of magnitude smaller than the slip rate in the steeply dipping segments. Such difference in slip rate may explain the lack of seismicity associated with low-angle detachment faults. The strong effect of fault-zone rheology on low-angle-detachment fault slip is also demonstrated. Modeling fault zones as thin-layer isotropic solids led to fault slip under a broader range of conditions than if the assumed fault-zone deformation was anisotropic and restricted to slip on fault-parallel planes.

15/10

INTRODUCTION

Yucca Mountain in Western Nevada is currently being considered for a mined geologic repository for the permanent disposal of nuclear waste under the United States high-level nuclear waste disposal program (Fig. 1). Because Yucca Mountain lies in the tectonically active Basin and Range Province containing numerous normal faults, one of the key technical issues associated with licensing and constructing a repository at the site is the evaluation of structural (geologic) deformation including the potential for displacement and seismicity on the existing faults.

There is considerable uncertainty regarding the subsurface fault geometry beneath the Yucca Mountain region (cf. [1]). Two alternative models of the subsurface fault geometry are shown in Fig. 2 (from [2]). The first model is based on the interpretation (after [3,4]) that normal faults beneath Yucca Mountain flatten with depth into a subhorizontal detachment. A cross section based on this interpretation was developed by Young et al. [1] using geometric balancing techniques. Such an interpretation explains the displacement magnitudes, fault block rotations, and differences in fault block rotations observed at the ground surface and in boreholes. In this model, the Yucca Mountain faults are interpreted as part of a west-dipping listric system with a detachment at a depth of 6–7 km, i.e., well within the brittle crust Fig. 2(a). An alternative interpretation (Fig. 2(b), from [2]) extends the Yucca Mountain faults steeply to the base of the Bare Mountain Fault at a depth of about 10–12 km, and within the brittle-ductile transition zone (e.g., [5]).

Normal faults that have listric shapes or are concave-upward in profile are a common

feature in extensional tectonic regions. Because of the fault shape, extension parallel to the low-angle segment of a listric normal fault necessitates deformation of the hangingwall, footwall, or both in order to maintain constant volume. Hamblin [6] interpreted listric fault geometry to explain the rollover that is commonly observed in the hangingwalls of normal faults. Models that involve only planar normal faults cannot easily explain such antithetic rotation of fault blocks [6]. Listric faults in the crust have been explained as follows:

1. High-angle faults merging at depth with weak (e.g., salt) or overpressured (e.g., shale) sedimentary horizons (e.g., [7]).

2. Synsedimentary extension and fault propagation that causes rotation of early formed fault segments to lower dips and upward propagation of faults at a high angle through newly deposited sediments [8].

3. Differential compaction increasing with depth, causing flattening of originally planar faults with depth [9].

4. High-angle faults that are rotated to lower angles as a result of footwall uplift [10].

5. Continuation of high-angle faults downward to the brittle/ductile transition, and horizontal detachment below the transition zone in the realm of ductile deformation [11–13].

6. Rotation of principal stress directions at mid-crustal depths, due to changes in rheology or stress associated with igneous intrusion, resulting in a 45° change in optimal fault dip (e.g., from steep dips of about 60° to gentle dips of about 15°) [14, 15].

M/10

The mechanical argument against listric normal faulting is that in regions of extensional faulting, in which the maximum principal compressive stress (σ_1) is vertical, new faults would be expected to form with steep dips. Under such stress conditions, the normal stress on a subhorizontal fault would be nearly equal to σ_1; as a result, the occurrence of slip on such faults cannot be explained with reference to a Mohr-Coulomb type strength criterion for the fault (cf. [16,17]).

Another argument against listric normal faulting arises from the fact that evidence for seismic slip on low-angle normal faults appears to be rare [18, 19]. The vast majority of earthquakes related to normal faulting occur in the depth range of 6 to 15 km on faults that dip between 30° and 60° [20]. The occurrence of earthquakes is largely dependent on the rate of slip or the rate of rupture propagation on a fault. Beroza and Jordan [21] illustrate that rupture propagation rates are typically in the range of kilometers per second for earthquakes, 10 to 1,000 m/s for slow and silent earthquakes, and less than 10 m/s for aseismic slip events. It has been suggested that the lack of seismicity on low-angle faults does not reflect lack of slip on the faults but instead that slip on such faults probably occurs at aseismic rates and may either precede or postdate seismic slip on high-angle portions of the fault [14].

In the current study, two-dimensional finite element analyses are performed on a cross section similar to the upper-crustal Yucca Mountain fault system modeled in Fig. 2(a). These analyses evaluate the effects of subsurface fault geometry on predictions of ground-surface deformations, fault displacement, ground accelerations associated with fault slip, and interactions among the various faults. A basic question examined in the analyses is whether

slip on one of the faults that belong to a listric fault system could trigger slip on the other faults within the system. In addition, the effects of *in situ* stress and material properties on the predicted response are examined through parametric analyses.

DESCRIPTION OF MODEL

Geometrical Model

The geometrical model used in the finite element analyses is illustrated in Fig. 3. The modeled domain is approximately rectangular, extending 43.5 km horizontally and 17.25 km vertically. Axis 1 in the figure (x-axis) extends eastward (i.e., horizontally), whereas axis 2 (y-axis) extends vertically up; the other horizontal axis, i.e., axis 3 (z-axis) extends northward. The ground surface was assumed to be horizontal at elevation 1.25 km above sea level (at a y-coordinate of 7250 m). All dimensions in the model are in meters. The modeled faults are referred to as the Gd, Br, FrPc, and Fmw fault zones, which are similar in attitude to the Ghost Dance Fault, Bow Ridge Fault, Fran Ridge and Paintbrush Canyon fault system, and the interpreted Fortymile Wash Fault, respectively, based on the modeled structural-geologic cross section (Fig. 2(a)). Each fault was represented as a 500-m thick zone of solid material that was assigned material properties different from those of the surrounding rock, as is explained later. The choice of thickness for the fault zones was influenced by finite-element meshing considerations, but may be justified considering field observations (cf. [4]) that suggest that the faults of interest in this study consist of zones of breccia and densely fractured rock up to 1 km wide.

Five stations selected for monitoring fault slip rate are shown in Fig. 3. Each of the stations (labeled Fm58, Fm168, Fr635, Br833, and Gd3194 in Fig. 3) is a finite element, and slip rate was monitored at the centroid of each element. The elements are located within zones where the largest values of slip were expected, based on observations from a series

of preliminary analyses. The region ABCD (shaded white) was selected to monitor stress changes induced by fault slip. The stress-change study zone covers a horizontal distance of about 10 km and extends vertically to a depth of about 1 km from the ground surface. The interest in such a zone arises from the possibility that the proposed repository may be located at a depth of about 300 m below the ground surface (cf. [1]). Figure 3 also shows the stations selected for monitoring ground accelerations, which are located within the epicentral zones of slip events that may originate near the base of the steeply dipping faults.

Material Model

The fault-zone materials were modeled as elastoplastic, with a yield strength defined in terms of the Drucker-Prager failure criterion [22]. A time-dependent stress-strain model was not selected because fault-zone deformations within the modeled depth range are expected to consist of brittle fracture rather than time-dependent plastic flow. The rest of the rock mass (i.e., the footwall of the Fmw zone and the part of the hangingwall outside the fault zones) was modeled as linear-elastic, homogeneous, and isotropic, with a constant Young's modulus $E = 32.5$ GPa and Poisson's ratio $\nu = 1/3$. Because deformations are expected to be localized within and close to the fault zones, uncertainties in the values of E and ν are not expected to have significant effects on the predicted response within the hangingwall. As a result, constant values were assigned to E and ν.

The same values of E and ν were also applied to the elastoplastic material zones. The additional parameters required for such zones are the unconfined compressive strength q_u, the Drucker-Prager friction angle β, and the dilation angle φ. For the conditions of plane

21/10

strain, the Drucker-Prager friction angle is related to the Mohr-Coulomb friction angle ϕ through the following equations, which vary depending on the ratio of the dilation angle to the friction angle [23]:

$$\tan\beta = \frac{\sqrt{3}\sin\phi}{\sqrt{1+\frac{1}{3\sin^2\phi}}} \qquad \text{for} \quad \varphi/\phi = 1 \tag{1}$$

$$\tan\beta = \sqrt{3}\sin\phi \qquad \text{for} \quad \varphi/\phi = 0 \tag{2}$$

The fault zones are expected to be essentially cohesionless; therefore, q_u was assigned a relatively small constant value of 1.0 MPa. The values of ϕ were varied in the range $30° \leq \phi \leq 40°$ (cf. [24]) and those of the ratio φ/ϕ were varied in the range $0 \leq \varphi/\phi \leq 1$.

An additional parameter (i.e., damping factor, D_α) is required in dynamic analyses to describe the material-damping response. Very little measured data exist on the damping property of rocks. Most of the data available for geologic materials, which were obtained for cohesionless soils, indicate D_α values of 0.01 to 0.1 (e.g., see Table 10-12 of [25]). The value of D_α for the fault zones was varied within the range of 0.01–0.1, which is consistent with the assumption that the fault zones consist of essentially cohesionless material. Analytical investigations ([26]) suggest that the value of D_α for geologic materials varies inversely with the shear modulus. Because the shear modulus of intact rock is several orders of magnitude larger than that of soils and unlithified sediments, the values of D_α for intact rock are likely to be very small. As a result, the linear-elastic zones were assigned zero material damping.

Initial Conditions

The medium was assumed to be under zero strain at the initial state, the justification for

the assumption being that the focus of the investigation is the mechanical changes induced by a perturbation of the current state. The strains associated with previous deformations of the medium are not relevant to the investigation, except to the extent that they may assist in defining the initial stress state. The ground surface was assumed to be horizontal, which implies that one of the principal compressive stress components is vertical and that the other two are horizontal. The ground-surface topography can affect the principal stress directions significantly, as is demonstrated in [27], for example. The assumption of horizontal ground surface was made to remove the ground-surface relief from the list of unknown variables, because it can be measured accurately and incorporated into subsequent analyses. The vertical principal compressive stress σ_v was computed using a vertical gradient of 25 MPa/km. Possible effects of vertical density variations on the vertical stress gradient were ignored, because it is believed that uncertainties related to the ratios of the principal stresses are likely to be more important than those related to the absolute magnitude of the vertical principal stress.

Because the Basin and Range Province is characterized by normal faulting, the maximum principal stress σ_1 is believed to be vertical (i.e., $\sigma_1 = \sigma_v$); also, the minimum principal compressive stress σ_3 is believed to be horizontal and normal to the strike of the fault planes (cf. [28]). Under such conditions, values of the ratio σ_3/σ_1 (denoted k_3) would lie in the range $k_a \leq k_3 \leq k_o$, where k_a is the value of the ratio for the condition of incipient failure under pure horizontal extension, and k_o is its value under the state of zero horizontal deformation (often referred to as the at-rest or uniaxial strain state [28]). The value of k_a is about 0.2 for a cohesionless material with a friction angle of about 40°; also, $k_o = 0.5$ for a Poisson's

23/10

ratio of 1/3. Such values of k_a and k_o were considered to represent reasonable end values, and therefore k_3 was varied between 0.2 and 0.5 for the parametric investigation. Such assumed values of k_3 are not necessarily intended to represent the actual values for the Yucca Mountain Region, but are simply used to determine the extent to which predictions from the model may be sensitive to k_3.

The magnitude of the intermediate principal stress σ_2 for the region is believed to be closer to that of σ_1 than to σ_3 (e.g., [29, 30]). Moreover, σ_2 has little influence in a two-dimensional analysis for which σ_1 and σ_3 lie in the plane of the analysis. As a result, σ_2 was assigned an initial-state value of $0.9\sigma_1$ for the current program of analyses.

Boundary Conditions

The top of the model coincides with the ground surface and was therefore treated as a free surface. The base of the model and the left and right boundaries of the Fmw-zone footwall were held at zero displacement in the direction normal to the boundary. A vertical downward pressure of 183.33 MPa was applied on the horizontal bench at the left end of the model. The left boundary of the model above this bench was subjected to a horizontal pressure equal to $0.025k_3d$ MPa, where d is the depth in meters. The primary consideration in selecting the minimum distance of the base and vertical boundaries of the model from the fault zones was the requirement that the calculated response should not be influenced by energy reflected from the boundaries (except the ground surface). This requirement could have been met by modeling the base and vertical boundaries with infinite elements, which have the built-in capability to reduce the reflection of dynamic energy. Although such elements may be

satisfactory for modeling the base, they are not designed for semi-infinite boundaries, such as occur at the intersection of the vertical boundaries with the ground surface. Secondly, because the infinite elements are based on the analytic behavior of a linear-elastic space, they are not satisfactory for modeling the left boundary of the Fmw fault zone. Therefore, the size of the model was increased to preclude boundary reflections, instead of using infinite elements at the boundaries.

Simulation Procedure

Each simulation was conducted in two steps, as follows. First, the initial equilibrium state was established through static analysis, considering the initial stress, gravitational forces, and boundary restraints. Second, slip was induced on a selected fault zone through dynamic analysis, simulating a single fault-slip event. The dynamic analysis was performed in increments, up to 0.01 s maximum, to permit detailed records of the induced ground acceleration. The selected response variables were monitored for a period of 5 s.

The method of inducing fault slip was initially intended to simulate the approach used in laboratory models of normal faulting, such as is illustrated in Fig. 4 (cf. [31]). In the laboratory experiment, the footwall consists of a rigid block and the hangingwall consists of deformable material (such as clay or loose sand) retained at its base by a metal or plastic sheet. For the example illustrated, slip would be induced by advancing the moveable wall to the right. The perturbation of the hangingwall represented by the moveable-wall displacement may be simulated numerically by applying a prescribed horizontal displacement at the exterior boundary of the hangingwall. However, for the problem illustrated in

Fig. 3, prescribed horizontal displacements at such a boundary would dissipate within the hangingwall without causing significant disturbance in the fault zones, because of the large distance between the fault zones and the exterior boundary of the hangingwall. A second problem with prescribing perturbations at the exterior boundary is that it results in an incorrect distribution of response magnitudes (such as displacements or stress change), with the largest magnitudes near the perturbed boundary. The appropriate location to apply prescribed perturbations is the fault on which slip is desired. Such perturbations may be applied in the form of distributed displacements or forces. For the simulations described in this paper, the prescribed perturbations consisted of an instantaneous reduction of the value of friction angle for a selected fault zone, to the value required for incipient slip based on the application of the Mohr-Coulomb failure criterion on planes parallel to the fault.

Numerical Experiment Design

Only one fault was perturbed at a time using the procedure described above. The perturbed faults are: (1) the upper (steep) segment of the Fmw zone, (2) the FrPc zone, (3) the Br zone, and (4) the entire Fmw zone. The response of the medium to such fault perturbations was expected to vary, depending on the values assigned to the input parameters k_3, ϕ, φ/ϕ, and D_α. Therefore, the numerical experiment consisted of monitoring the response of the medium to fault slip under several combinations of the four input parameters and the perturbed fault.

The response was monitored in terms of the following variables: (1) Fault displacement, D_f, on each of the four fault zones. (2) Slip rate, S_r, at each of the five slip-rate monitoring

stations shown in Fig. 3. (3) Slip length, L_s, on each of the four fault zones. (4) Limit-equilibrium friction angle (ϕ_{lim}), i.e., the smallest friction angle that would prevent slip, on each of the four fault zones. (5) Maximum vertical and horizontal accelerations, a_v and a_h, respectively, at each of the six acceleration-monitoring stations shown in Fig. 3. (6) Area, A, of the zone of potential instability within the study zone (white rectangular region in Fig. 3), considering the occurrence of slip on planes dipping 65°, 75°, and 80°, each having a friction angle of 30° or 40°.

The input-parameter combinations were generated in terms of the normalized values of k_3, ϕ, φ/ϕ, and D_α. The normalized value, θ_r, of a given variable θ was defined in terms of its maximum and minimum values, θ_{max} and θ_{min}, respectively, as follows:

$$\theta_r = \frac{\theta - \theta_{\text{min}}}{\theta_{\text{max}} - \theta_{\text{min}}} \tag{3}$$

This equation gives values of θ_r in the range $0 \leq \theta_r \leq 1$. Seventeen combinations of values of four θ_r-type variables were generated randomly and converted to values of k_3, ϕ, φ/ϕ, and D_α using the inverse of Eq. 3. Each of the 17 combinations was then applied to the perturbation of the four faults, giving a total of 68 simulations.

27/70

DESCRIPTION OF CALCULATED RESULTS

Distributions of Stressess and Deformations

Distributions of displacement vectors are presented in Figs. 5 and 6, representing the conditions at the end of 5 s following the perturbation of the Fmw and Br fault zones, respectively. The input-parameter values for the cases shown in the figures are $k_3 = 0.4$, $\phi = 30°$, $\varphi/\phi = 0.1$, and $D_\alpha = 0.05$. As the figures show, the displacement pattern associated with each fault slip consists of upward-eastward displacements on the footwall and downward-westward displacements on the hangingwall. This displacement pattern is consistent with the occurrence of normal faulting on the perturbed fault. The ground-surface profile across the Br fault zone is shown in Fig. 7 for the second analysis case (perturbation of the Br fault with the above input values). As the figure shows, the calculated ground-surface profile includes footwall uplift and hangingwall rollover that decrease in magnitude away from the fault, both of which are common features associated with slip on listric normal faults.

The perturbed fault and the low-angle segment of the Fmw fault are shown in white in Figs. 5 and 6 to emphasize the relationships of the fault zones to the displacement-vector orientations. The hangingwall displacement vectors associated with slip on the Fmw fault zone (Fig. 5) generally follow the orientation of the fault in the high-angle segment and in the high-to-low angle transition segment. On the other hand, the hangingwall displacement vectors associated with slip on the FrPc and Br fault zones (as shown in Fig. 6, for example) follow the orientation of the faults in the steeply dipping segments only. The vectors are curved in the zone of intersection of the faults with the low-angle detachment, suggesting that

the transition from the steep to low-angle faults is more gradual for these two faults than is represented in the current model. The transitions are indeed shown as gradual in Fig. 2, but were modeled as abrupt in this study, in order to examine the effects of fault shape on the distribution and orientations of slip. Curvilinear slip patterns for abrupt angular changes in fault dip suggest that such angular fault intersections may evolve to more curvilinear shapes.

It is also noted that the displacement vectors in the low-angle detachment are generally inclined to the fault, have a downward-westward sense, and are large relative to those in the neighboring areas of the footwall. Such a distribution of displacement vectors is consistent with the occurrence of oblique slip planes inclined to the fault at angles of about 30° within the low-angle detachment. The occurrence of such slip planes or shear zones, referred to as Riedel shears (cf. [32]), has been described in the geological literature [33]. An example of Riedel shears associated with a mining-induced seismic event was reported in [34]. This observation regarding possible occurrence of Riedel shears in the low-angle detachment suggests that oblique slip planes also need to be considered in assessing the potential for slip on listric normal faults. This result also suggests that an isotropic strength criterion, such as was applied in this study, better simulates the mechanical behavior of listric normal fault zones than would a strength criterion that restricts inelastic response to fault-parallel planes.

The distribution of plastic strain associated with the perturbation of the Fmw fault zone (in the same analysis case presented in Fig. 5) is shown in Fig. 8 in terms of the magnitude of plastic strain Γ^P, defined as follows:

$$\Gamma^P = \sqrt{\frac{2}{3}\left[(e_{11}^P)^2 + (e_{22}^P)^2 + (e_{33}^P)^2 + 2(e_{12}^P)^2\right]} \tag{4}$$

29/70

where e_{ij}^{P} is the plastic strain tensor. As Fig. 8 shows, the magnitude of plastic strain is largest in the steep segments and smallest in the low-angle segments of the listric fault. Typically, slip initiated near the base of the steep segment and propagated upward toward the ground surface and downward toward the detachment. Such a pattern of slip propagation is consistent with the initiation of seismic events deep within the crust and upward propagation of the associated faults toward the ground surface. Also, results are presented later to suggest that slip in the low-angle detachment may occur at aseismic rates in association with possible seismic slips in the steep segments.

Figures 9 and 10 show the distributions of maximum and minimum principal stresses associated with the same analysis (presented in Fig. 8). The values of stress in the figures are presented using the tension-positive sign convention. The nature and magnitude of stress change (relative to the initial state) represented by the stress distributions are directly related to the nature and amount of departure of the stress contours from horizontal. As the figures show, a general increase in compressive stress occurred within the fault zones, especially in the low-angle detachment and high-to-low angle transition segments. The minimum principal stress increased more than the maximum principal stress, indicating that fault slip caused the differential stress ($\sigma_1 - \sigma_3$) within the fault zone to decrease. The magnitudes of stress change are much larger in the fault zones than in the linear elastic zones, as is shown by the discontinuity in the stress distributions.

Fault Displacement

Generally, fault displacement refers to the magnitude of permanent relative displacement

between the hangingwall and footwall, measured in a direction parallel to the fault. Its value generally varies along the dip of a fault, because of the internal deformation of the hangingwall and footwall. For the analyses described in this paper, it was necessary to define fault displacement in a way that permits its quick evaluation, because of the large number of simulations conducted. The modified definition was acceptable because the objective of the analyses was to examine how the calculated response varied between the different simulations, in which case the absolute magnitude of fault displacement calculated in any one simulation was not really important. As a result, fault displacement was defined as follows:

$$D_f = \sum_{n=1}^{N} (l_t \varepsilon_t)_n \tag{5}$$

where l_t is the length of a finite element in the tangential direction of the fault, ε_t (referred to as the tangential plastic strain) is the plastic shear strain component parallel to the fault at the centroid of the element, and N is the total number of elements along the fault. Each fault zone was modeled using three fault-parallel layers of finite elements, and equation (5) was applied to the middle layer. The parameter D_f is the total displacement along the fault; the average fault displacement is equal to D_f/N. The tangential plastic strain was calculated through a transformation of the plastic strain tensor, e_{ij}^P, using the following equation (cf. [28]):

$$\frac{\varepsilon_t}{2} = \frac{1}{2}(e_{22}^P - e_{11}^P)\sin 2\alpha + e_{12}^P \cos 2\alpha \tag{6}$$

where $\alpha = \psi + \pi/2$ and ψ is the dip of the fault. Typical profiles of tangential plastic strain are shown in Figs. 11 and 12, which show that a large fraction of the fault displacement

occurs over a small fraction of the total fault length along the dip of the fault. Most of the displacement occurred in the steeply dipping fault segments. As a result, the displacement distribution is much less uniform on the listric fault (Fmw fault zone) than on the planar faults (FrPc and Br fault zones). Such nonuniform distributions of fault displacement imply significant deformations of the hangingwall and footwall that increase in severity as the nonuniformity of the fault-displacement distribution increases. As a result, slip on listric faults (such as the Fmw fault) cause more severe deformations of the hangingwall and footwall than does slip on planar faults (such as the FrPc and Br faults).

Slip Rate

The history of slip was monitored at the five stations identified in Fig. 3, each of which is the centroid of a finite element. The stations were chosen to monitor the rate of slip within the base of the steep segment of the Fmw fault zone (Station Fm168), the base of the FrPc, Br, and Gd fault zones (Stations Fr635, Br833, and Gd3194, respectively), and the low-angle detachment (Station Fm58). In each case, the slip at the element centroid was calculated as the product $l_t\varepsilon_t$ in equation (5), and the slip rate S_r was calculated through a numerical differentiation of the slip history. The slip-rate history for Station Fm168 under simulation case c52 (with material parameters $k_3 = 0.4$, $\phi = 37.5°$, $\varphi/\phi = 0.75$, and $D_\alpha = 0.05$; and the entire Fmw fault zone as the perturbed fault) is shown in Fig. 13. The response shown in the figure is typical of the slip-rate response observed for all cases of slip on a fault induced by a perturbation of the same fault. In all such cases, the slip response consists of an instantaneous rupture at a rate of about 15–35 m/s, followed by several seconds of

movement at relatively slow and progressively decreasing rates.

The following conclusions arise from an examination of the range of values of slip rate calculated at the monitored stations [35]: (1) The rates of induced slip (i.e., slip in a fault caused by a perturbation of the same fault as defined earlier) are generally about three orders of magnitude larger than the rates of triggered slip (i.e., slip on a fault caused by the induced slip in another fault). For example, whereas the maximum slip rate at Station Fm168 (within the steep segment of the Fmw fault zone) is 31 m/s for cases of Fmw-zone perturbation, the maximum rate of triggered slip at the same station is only about 0.01 m/s. (2) The rates of induced slip in the low-angle detachment are up to two orders of magnitude smaller than the rates of induced slip in the steep segments of the same fault. (3) The rates of triggered slip in the low-angle detachment associated with the perturbation of any of the steeply dipping faults (i.e., the Br, FrPc, or steep segment of Fmw fault zones) is about six orders of magnitude smaller than the rates of the induced slip.

One possible significance of these observations relates to the classification of lithospheric deformations suggested in [21], according to which deformational events are classified as seismic or aseismic, depending on their associated rupture velocity. Based on this classification, silent earthquakes are associated with rupture rates of 10–100 m/s, slow earthquakes with 100–1000 m/s, whereas ordinary earthquakes occur at rupture rates larger than 1000 m/s. Deformational events associated with smaller rates of rupture are classified as creep events (rupture rates of 1 cm/s through 1 m/s) or strain migration (rupture rates less than 1 cm/s). These values suggest a 1–4 order-of-magnitude difference between the rupture rates

33/10

associated with the slowest seismic events (silent earthquakes) and the fastest aseismic events (creep). Therefore, the six order-of-magnitude difference between the slip rates in the low-angle detachment fault and steeply dipping faults suggests that low-angle detachments are likely to slip aseismically in response to seismic slip events in steeply dipping fault segments.

Slip Length

The importance of slip length lies in its potential for estimating earthquake magnitude [36]. However, in this study slip events were not converted to earthquake magnitudes for the following reasons. First, the distribution of forces that corresponds to the applied friction-angle reduction was not determined. Second, as shown in Figs. 11 and 12, the distribution of slip on the faults is nonuniform, and, more important, each slip event consisted of a short period of high slip rate followed by a much longer period of lower slip rates (probably aseismic). As a result, it is not yet clear how much of the calculated slip length may be used for earthquake-magnitude calculation.

Given these limitations, the slip length was monitored only for the purpose of examining the sensitivity of the monitored responses to changes in values of input parameters. It was defined as the total length of a fault over which a tangential plastic strain, ε_t, of at least 1.0×10^{-5} occurred. The following conclusions arise from an examination of the range of values of the calculated slip length [35]: (1) Self-induced slips, that is, slip induced on a fault by a perturbation of the same fault, occurred over the entire length of the fault. As a result, the self-induced slip lengths are independent of the input parameters. (2) The perturbation of the Fmw fault zone has stronger effects than the perturbation of either the

FrPc or Br fault zones. For example, whereas slip lengths on the Gd fault zone induced by the perturbation of the Fmw fault attained a maximum of about 2 km, the maximum slip length caused on the Gd zone by a perturbation of either the FrPc or Br faults is only about 0.5 km. (3) Slips induced on a fault due to the perturbation of another fault initiated either at the ground surface or at depth near the base of the fault. All the induced slip on the Gd fault zone initiated at the ground surface and extended to depths of between 0.5 and 2.0 km, which, as discussed below, is consistent with the distribution of stress change within the study zone.

Limit-Equilibrium Friction Angle

The limit-equilibrium friction angle, ϕ_{lim}, for a rock interface is the value of friction angle that would satisfy the Mohr-Coulomb condition for incipient slip under the existing stress state. If the value of ϕ_{lim} is smaller than the actual value of friction angle for the interface, then slip is not likely; on the other hand, slip is predicted if the calculated ϕ_{lim} is equal to or larger than the friction angle for the interface. The values of ϕ_{lim} were calculated as $\arctan \tau/\sigma_n$, where τ and σ_n are the shear and normal stresses, respectively, on a plane parallel to the fault (compare with *slip tendency* in [2]).

An examination of the calculated range of values of ϕ_{lim} [35] leads to two observations. First, the largest value of ϕ_{lim} occurred on the Fmw fault zone. Second, for the other faults, the largest values of ϕ_{lim} were associated with the perturbation of the Fmw fault zone, which reinforces an observation made earlier that the perturbation of the Fmw fault produced more severe effects than the perturbation of any of the other faults.

35/70

Ground Accelerations

The values of induced ground acceleration may be calculated using a numerical model, either to predict the magnitudes of acceleration that may be associated with a predetermined slip on a predetermined fault, or to verify the fault geometries obtained from fault-plane solutions of known earthquakes. In this study, vertical and horizontal accelerations were monitored at the six locations identified in Fig. 3. Four of the stations are located on the ground surface and the other two at depths of about 300 m below the ground surface. All the stations lie approximately within the epicentral area of slip events originating from the base of the Br, FrPc, or steep segment of the Fmw fault zones. The acceleration histories associated with the perturbation of the entire Fmw zone in simulation case c64 (with input-parameter values of $k_3 = 0.26$, $\phi = 32°$, $\varphi/\phi = 0.3$, and $D_\alpha = 0.02$), are given in Figs. 14 and 15, for Stations 2537 and 5661, respectively. The figures show differences in the arrival time, maximum acceleration, and frequency content of the seismic event as recorded at the two stations. The strongest vibrations associated with the event originated from the steep segment of the Fmw fault zone; as a result, Station 2537 is considered to be closer to the epicentral area than the other station, which would explain the differences in the arrival times and frequency content observed at the two stations. Events originating from the low-angle detachment would cause stronger ground motions at Station 5661 than at Station 2537, considering the distance of the stations from the detachment. Therefore, the relatively large magnitude of horizontal acceleration observed at Station 5661 is believed to be caused by the superposition of ground motions originating from the low-angle detachment and those originating from the steep segment of the Fmw fault zone. Two observations

are made considering the calculated range of values of maximum vertical and horizontal accelerations [35]. First, the perturbation of either the entire Fmw fault zone or the steep segment of the fault alone caused larger ground motions at the acceleration stations than the perturbation of the Br or FrPc fault zones. Second, the magnitudes of ground acceleration calculated at a location on the ground surface exceeded the acceleration at a depth of about 300 m below the same location by up to 1 m/s^2.

Stress Distributions in the Stress-Change Study Zone

The stress conditions within the stress-change study zone (area ABCD in Fig. 3) were processed to determine if such stresses would cause slip to occur on planar discontinuities within this zone that were not included in the model. Three sets of discontinuities, dipping at 65°, 75°, and 80°, west, were considered. The slip tendency for the discontinuities was assessed in terms of the values of the limit-equilibrium friction angle, ϕ_{lim}. The distribution of ϕ_{lim} for the 75°-dipping plane is given in Fig. 16 (top plot) for simulation case c61 (with input-parameter values of $k_3 = 0.26$, $\phi = 32°$, $\varphi/\phi = 0.3$, and $D_\alpha = 0.02$; and the steep segment of the Fmw fault zone as the perturbed fault). The figure shows the regions of the study zone within which the value of ϕ_{lim} is smaller than 30°, between 30° and 40°, or larger than 40°. The zone of $\phi_{\text{lim}} \geq 40°$ represents the potentially unstable zone based on the slip tendency for planar features having a friction angle of 40°. Similarly, the $\phi_{\text{lim}} \geq 30°$ zone represents the potentially unstable zone considering planes having a friction angle of 30°.

The distributions of vertical and horizontal stresses corresponding to the ϕ_{lim}-distribution are also given in Fig. 16 (middle and bottom plots, respectively). The nature and magnitude

of the stress change are directly related to the nature and amount of departure of the stress contours from horizontal. As the figure shows, the magnitude of vertical compressive stress increased, whereas the horizontal one decreased, relative to the initial stress in the area of the study zone west of the Gd fault zone. This zone corresponds corresponds to the zone of potential instability identified in the figure as discussed in the preceding paragraph.

The spread of potential instability in the study zone was measured in terms of the area of the $\phi_{\text{lim}} \geq 30°$ zone (representing the case of planar discontinuities that have friction angle of 30°), and the area of the $\phi_{\text{lim}} \geq 40°$ zone. An examination of the calculated range of values for these areas [35] leads to the following observations. First, the spread of potential instability caused by the perturbation of the Fmw fault zone is much larger than that caused by the perturbation of the Br or FrPc fault zones. Second, for planar discontinuities dipping more than 60°, the area of potential instability due to slip on the planes decreases as the magnitude of dip increases. This case occurs only when the principal stresses are vertical and horizontal and instability is related to slip alone. Under such a stress state, the magnitude of shear stress on the planes approaches zero as the dip approaches 90°, and, as a result, near-vertical planes are more likely to open than they are to slip.

SENSITIVITY OF RESPONSE VARIABLES TO INPUT PARAMETERS

A sensitivity analysis of the calculated responses was conducted to identify the input parameters that have dominant effects on the response variables. The analysis was based on scatter plots of the response variables versus the input parameters, both normalized according to equation (3). Such plots were used to determine potentially significant correlations between pairs of response and input variables, based on visual examination only. For example, Figs. 17 and 18 show the sensitivity of the total fault displacement in the Fmw fault zone, $D_{f(\mathrm{Fmw})}$, to changes in the values of k_3 and ϕ, respectively. As the two figures show, whereas significant correlation occurs between $D_{f(\mathrm{Fmw})}$ and k_3, there is no discernable correlation between $D_{f(\mathrm{Fmw})}$ and ϕ. This method of sensitivity analysis was adopted because the input parameters k_3, ϕ, φ, and D_α are believed to be independent of each other.

A correlation between a pair of response variable and input parameter implies that the variability of the particular input parameter has a dominant effect on the predicted values of the response variable. On the other hand, the absence of significant correlation implies that any effect of the variability of the input parameter on the response variable is overshadowed by the variability of other input parameters. This distinction between input parameters that have a dominant effect and those that do not leads to recommendations regarding the input parameters that can be assigned single values and those whose values need to be varied within a range, in an analysis to predict values of a selected response variable. For example, the results presented in Figs. 17 and 18 imply that the parameter ϕ may be assigned a single value whereas k_3 needs to be varied to examine its effect in an analysis to evaluate

the response variable $D_{f(\mathrm{Fmw})}$.

The results of the sensitivity analysis, presented in detail in [35], are summarized in Table 1. In the table, each response-variable designation consists of the symbol assigned earlier combined with a subscript that indicates the fault or monitoring station at which the variable was evaluated. For example, $D_{f(\mathrm{Fmw})}$ stands for total fault displacement on the Fmw fault zone, $a_{v(2537)}$ stands for vertical acceleration at station 2537, and $A_{(\phi=40,\psi=80)}$ stands for the area of potential instability within the study zone based on the slip tendency for 80°-dipping planar discontinuities with friction angle of 40°. Each bullet in the table indicates a pair of response variable and input parameter for which correlation was judged to occur based on a plot such as Fig. 17. The non-bulleted pairs are those for which the plots indicate no significant correlation, such as Fig. 18.

The results presented in Table 1 lead to the following conclusions: (1) The variability of the *in situ* stress ratio k_3 has a dominant effect on the predicted hangingwall response, except the magnitudes of ground acceleration. (2) The variability of the damping factor D_α has a dominant effect on the predicted ground accelerations within the hangingwall. (3) The effects of the variabilities of ϕ, φ/ϕ, and D_α on all aspects of hangingwall response except ground accelerations are overshadowed by the effects of the variability of k_3. (4) The effects of the variabilities of k_3, ϕ, and φ/ϕ on ground accelerations are overshadowed by the effects of the variability of D_α. Therefore, in an analysis to predict the values of ground acceleration, each of the parameters k_3, ϕ, and φ/ϕ may be assigned a single value whereas the effects of varying D_α should be examined. For analyses to predict other aspects of hangingwall

response, the effects of the variability of k_3 should be examined, but the parameters ϕ, φ/ϕ, and D_α may each be assigned a single value.

Table 1: Sensitivity of response variables to input parameters. Numbers 1, 2, 3, and 4 indicate perturbed fault (upper Fmw, FrPc, Br, and entire Fmw, respectively). Bullet indicates significant correlation between a response variable and an input parameter.

Variable	k_3				ϕ				φ/ϕ				D_α			
	1	2	3	4	1	2	3	4	1	2	3	4	1	2	3	4
$D_{f(\mathrm{Fmw})}$	•	•	•	•												
$D_{f(\mathrm{FrPc})}$		•														
$D_{f(\mathrm{Br})}$	•		•	•												
$D_{f(\mathrm{Gd})}$	•			•					•			•	•			•
$S_{r(\mathrm{Gd3194})}$	•	•	•	•												
$S_{r(\mathrm{Br833})}$	•	•	•													
$S_{r(\mathrm{Fr635})}$	•	•	•													
$S_{r(\mathrm{Fm168})}$			•													
$S_{r(\mathrm{Fm58})}$	•	•	•	•												
$L_{s(\mathrm{Fmw})}$	•	•	•	•												
$L_{s(\mathrm{FrPc})}$																
$L_{s(\mathrm{Br})}$	•			•								•				
$L_{s(\mathrm{Gd})}$	•			•					•			•	•			•
$\phi_{\mathrm{lim}(\mathrm{Fmw})}$		•	•			•	•									
$\phi_{\mathrm{lim}(\mathrm{FrPc})}$	•		•	•	•		•	•								
$\phi_{\mathrm{lim}(\mathrm{Br})}$	•	•		•	•	•		•								
$\phi_{\mathrm{lim}(\mathrm{Gd})}$	•	•	•	•												

Table 1: contd.

Variable	k_3				ϕ				φ/ϕ				D_α			
	1	2	3	4	1	2	3	4	1	2	3	4	1	2	3	4
$a_{v(2537)}$													•	•	•	•
$a_{v(5476)}$													•	•	•	•
$a_{v(5596)}$													•	•	•	•
$a_{v(5597)}$													•	•	•	•
$a_{v(5661)}$													•	•	•	•
$a_{v(5662)}$													•	•	•	•
$a_{h(2537)}$													•	•	•	•
$a_{h(5476)}$													•	•	•	•
$a_{h(5596)}$													•	•	•	•
$a_{h(5597)}$													•	•	•	•
$a_{h(5661)}$													•	•	•	•
$a_{h(5662)}$													•	•	•	•
$A_{(\phi=30,\psi=65)}$	•	•	•	•												
$A_{(\phi=30,\psi=75)}$	•	•	•	•												
$A_{(\phi=30,\psi=80)}$	•	•	•	•												
$A_{(\phi=40,\psi=65)}$	•	•	•	•												
$A_{(\phi=40,\psi=75)}$	•	•	•	•												
$A_{(\phi=40,\psi=80)}$	•	•	•	•												

43/70

CONCLUSIONS

1. The values of *in situ* stress used in the analyses of hangingwall deformations deserve particular attention. For such analyses, *in situ* stress data are required, preferrably based on measurements at depths below the zone of influence of ground-surface topography, in order to define the range of values of the initial principal stress ratios.

2. For analyses to predict the values of ground acceleration, it is necessary to constrain damping as much as possible, and then to evaluate the range of accelerations for the range of accepted values of the material damping factor.

3. Slip on a broadly curved fault with dip that changes gradually from steep to low-angle has greater impact on hangingwall deformation than slip on steeply dipping faults that terminate abruptly at a low-angle detachment. For example, in the Yucca Mountain Region, the modeling indicates that slip on the interpreted Fortymile Wash Fault produced greater impact on hangingwall deformation than did slip on the other faults.

4. Slip rates in the low-angle segments of the modeled listric fault system were found to be several orders of magnitude smaller than the associated slip rates in the steep segments. Such differences in slip rate may explain the lack of seismicity associated with low-angle faults. Slip on low-angle faults appear to occur at aseismic rates and can either precede or postdate seismic slip on the steeper fault segments.

5. The best approach to modeling listric faults contained entirely in the brittle crust is to represent each fault as a thin, relatively weak zone with isotropic properties.

ACKNOWLEDGEMENTS

The work described in this paper was performed at the Center for Nuclear Waste Regulatory Analyses (Southwest Research Institute, San Antonio, Texas) for the United States Nuclear Regulatory Commission (NRC) under contract number NRC-02-93-005. The work was done on behalf of the NRC Office of Nuclear Material Safety and Safeguards, Division of Waste Management. The views expressed in the paper are those of the authors and do not necessarily reflect the views or regulatory position of the NRC.

The authors are grateful to S. Young, R. Hofmann, A.P. Morris, and H.L. McKague for technical contributions made at various stages of the project. The finite element analyses described in this paper were conducted using ABAQUS [23].

References

1. Young, S. R., Stirewalt, G. L., and Morris, A. P. Geometric models of faulting at Yucca Mountain. Technical Report CNWRA 92-008, Center for Nuclear Waste Regulatory Analyses, San Antonio, TX (1992).

2. Ferrill, D. A., Stirewalt, G. L., Henderson, D. B., Stamatakos, J. A., Morris, A. P., Wernicke, B. P., and Spivey, K. Faulting in the Yucca Mountain Region: Critical review and analyses of tectonic data from the Central Basin and Range. Technical Report CNWRA 95-017, Center for Nuclear Waste Regulatory Analyses, San Antonio, TX (1995).

3. Scott, R. B. and Bonk, J. Preliminary geologic map of Yucca Mountain, Nye County, Nevada, with geologic sections. 1:12000. Technical Report USGS-OFR-84-494, U. S. Geological Survey (1984).

4. Scott, R. B. Tectonic setting of Yucca Mountain, southwestern Nevada. In Basin and Range Extensional Tectonics Near the Latitude of Las Vegas, Nevada, Wernicke, B. P., Ed., *Geol Soc Am Mem*,**176**, 251–282 (1990).

5. Gilmore, T. D. Geodetic leveling data used to define historical height changes between Tonopah Junction and Las Vegas, Nevada. Technical Report USGS-OFR-92-450, U. S. Geological Survey (1992).

6. Hamblin, W. K. Origin of "reverse drag" on the downthrown side of normal faults. *Geol Soc Am Bull*, **76**, 1145–1164 (1965).

7. Vendeville, B. Mechanisms generating normal fault curvature: a review illustrated by physical models. In The Geometry of Normal Faults, Roberts, A. M., Yielding, G., and Freeman, B., Eds., *Spec Publ Geol Soc London*,**56**, 241–249, (1991).

8. Vendeville, B. and Cobbold, P. R. How normal faulting and sedimentation interact to produce listric fault profiles and stratigraphic wedges. *J Struct Geol*, **10**, 649–659 (1988).

9. Xiao, H. B. and Suppe, J. Role of compaction in listric shape of growth normal faults. *Am Assoc Pet Geol Bull*, **73**, 777–786 (1989).

10. Wernicke, B. and Axen, G. J. On the role of isostacy in the evolution of normal fault systems. *Geology*, **16**, 848–851 (1988).

11. Wernicke, B. and Burchfiel, B. C. Modes of extensional tectonics. *J Struct Geol*, **4**, 105–115 (1982).

12. Miller, E. L., Gans, P. B., and Garing, J. The Snake Range decollement: An exhumed mid-Tertiary ductile-brittle transition. *Tectonics*, **2**, 239–263 (1983).

13. Allmendinger, R. W., Hauge, T. A., Hauser, E. C., Potter, C. J., Klemperer, S. L., Nelson, K. D., Knuepfer, P., and Oliver, J. Overview of the COCORP 40°N Transect, western United States: The fabric of an orogenic belt. *Geol Soc Am Bull*, **98**, 308–319 (1987).

14. Melosh, H. J. Mechanical basis for low-angle normal faulting in the Basin and Range Province. *Nature*, **343**, 331–335 (1990).

47/70

15. Parsons, T. and Thompson, G. A. Does magmatism influence low-angle normal faulting? *Geology*, **21**, 247–250 (1993).

16. Sibson, R. H. A note on fault reactivation. *J Struct Geol*, **7**, 751–754 (1985).

17. Ferrill, D. A., Morris, A. P., Henderson, D. B., and Martin, R. H. Tectonic processes in the central Basin and Range region. In NRC High-Level Radioactive Waste Research at CNWRA, July-December 1994, Sagar, B., Ed., 121–139. Center for Nuclear Waste Regulatory Analyses, San Antonio, TX (1995).

18. Abers, G. A. Possible seismogenic shallow-dipping normal faults in the Woodlark-D'Entrecasteaux extension province, Papua New Guinea. *Geology*, **19**, 1205–1208 (1991).

19. Johnson, R. A. and Loy, K. L. Seismic reflection evidence for seismogenic low-angle faulting in southeastern Arizona. *Geology*, **20**, 597–600 (1992).

20. Jackson, J. A. Active normal faulting and crustal extension. In Continental Extensional Tectonics, Coward, M. P. et al., Eds., *Spec Publ Geol Soc London*,**28**, 3–17 (1987).

21. Beroza, G. C. and Jordan, T. H. Searching for slow and silent earthquakes using free oscillations. *J Geophys Res*, **95**(B3), 2485–2510 (1990).

22. Drucker, D. C. and Prager, W. Soil mechanics and plastic analysis of limit design. *Quart Appl Math*, **10**(2), 157–172 (1952).

23. Hibbit, Karlsson and Sorensen, Inc. *ABAQUS Users' Manual, Version 5.4*, Pawtucket, RI (1994).

24. Byerlee, J. Friction of rocks. *Pure Appl Geophys*, **116**, 615–626 (1978).

25. Richart, F. E., Woods, R. D., and Hall, J. R. *Vibrations of Soils and Foundations.* Prentice-Hall, Englewood Cliffs, NJ (1970).

26. Hardin, B. O. The nature of damping in sands. *Am Soc Civ Eng Proc J Soil Mech Found Div*, **91**(SM1), 63–97 (1965).

27. Goodman, R. E. *Introduction to Rock Mechanics.* John Wiley and Sons, New York, NY (1980).

28. Jaeger, J. C. and Cook, N. G. W. *Fundamentals of Rock Mechanics.* Chapman and Hall, London, third edition (1979).

29. Harmsen, S. C. The Little Skull Mountain, Nevada, earthquake of 29 June 1992: Aftershock focal mechanisms and tectonic stress field implications. *Bull Seism Soc Am*, **84**(5), 1484–1505 (1994).

30. Stock, J. M., Healy, J. H., Hickman, S. H., and Zoback, M. D. Hydraulic fracturing stress measurements at Yucca Mountain, Nevada, and relationship to regional stress field. *J Geophys Res*, **90**(B10), 8691–8706 (1985).

31. Withjack, M. O., Islam, Q. T., and La Pointe, P. R. Normal faults and their hanging-wall deformation: an experimental study. *Am Assoc Pet Geol Bull*, **79**, 1–18 (1995).

49/70

32. Skempton, A. W. Some observations on tectonic shear zones. *Int Soc Rock Mech Congr Proc*, **1**, 329–335 (1966).

33. Groshong, Jr., R. H. Low-temperature deformation mechanisms and their interpretation. *Geol Soc Am Bull*, **100**, 1329–1360 (1988).

34. Gay, N. C. and Ortlepp, W. D. Anatomy of a mining-induced fault zone. *Geol Soc Am Bull*, **90**, 47–58 (1979).

35. Ofoegbu, G. I. and Ferrill, D. A. Finite element modeling of listric normal faulting. Technical Report CNWRA 95-008, Center for Nuclear Waste Regulatory Analyses, San Antonio, TX (1995).

36. Wells, D. L. and Coppersmith, K. J. New empirical relationships among magnitude, rupture length, rupture width, rupture area, and surface displacement. *Bull Seism Soc Am*, **84**, 974–1002 (1994).

List of Figures

1 Map of Yucca Mountain area showing proposed repository area. Dimensions are UTM coordinates.

2 Geologic cross section along path BC (Fig. 1) based on two alternative models for Yucca Mountain faults [2]

3 Geometrical model showing boundaries of the modeled domain and fault zones. Stress change was monitored within region ABCD with corners at A(2024, 7250), B(1911, 6104), C(11981, 6360), and D(12005, 7250) m. Dark dots within the stress-change study zone represent the acceleration-monitoring stations.

4 Schematic illustration of typical approach used to simulate normal faulting in laboratory experiments. Adapted from [31].

5 Distribution of displacement vectors associated with slip on the Fmw fault zone. Arrow lengths normalized with respect to maximum displacement of 1.018 m.

6 Distribution of displacement vectors associated with slip on the Br fault zone. Arrow lengths normalized with respect to maximum displacement of 1.427 m.

7 Ground-surface profile associated with slip on the Br fault zone.

8 Distribution of plastic-strain magnitudes associated with slip on the Fmw fault zone.

51|10

9 Distribution of maximum principal compressive stress associated with slip on the Fmw fault zone.

10 Distribution of minimum principal compressive stress associated with slip on the Fmw fault zone.

11 Typical distributions of fault slip along the Fmw fault zone.

12 Typical distributions of fault slip along the FrPc and Br fault zones.

13 History of slip rate at Station Fm168 under simulation case with parameters $k_3 = 0.4$, $\phi = 37.5°$, $\varphi/\phi = 0.75$, and $D_\alpha = 0.05$; and the entire Fmw fault zone as the perturbed fault.

14 Acceleration history at Station 2537 (located on the ground surface east of the FrPc fault zone in Fig. 3) under simulation case with parameters $k_3 = 0.26$, $\phi = 32°$, $\varphi/\phi = 0.3$, and $D_\alpha = 0.02$; and the entire Fmw fault zone as the perturbed fault.

15 Acceleration history at Station 5661 (western-most ground-surface station in Fig. 3) under simulation case with parameters $k_3 = 0.26$, $\phi = 32°$, $\varphi/\phi = 0.3$, and $D_\alpha = 0.02$; and the entire Fmw fault zone as the perturbed fault.

16 Distributions of potential instability based on the slip tendency for 75°W-dipping planar discontinuities (top plot), vertical stress (middle plot), and horizontal stress (bottom plot). Plots cover the area ABCD in Fig. 3 (with faults extended below the area to indicate their locations) and are based on a perturbation of the Fmw-fault steep segment with parameters $k_3 = 0.26$, $\phi = 32°$, $\varphi/\phi = 0.3$, and $D_\alpha = 0.02$. White space between faults should be ignored.

17 Sensitivity of total fault displacement in the Fmw fault zone to changes in the value of the principal stress ratio k_3

18 Sensitivity of total fault displacement in the Fmw fault zone to changes in the value of the friction angle ϕ

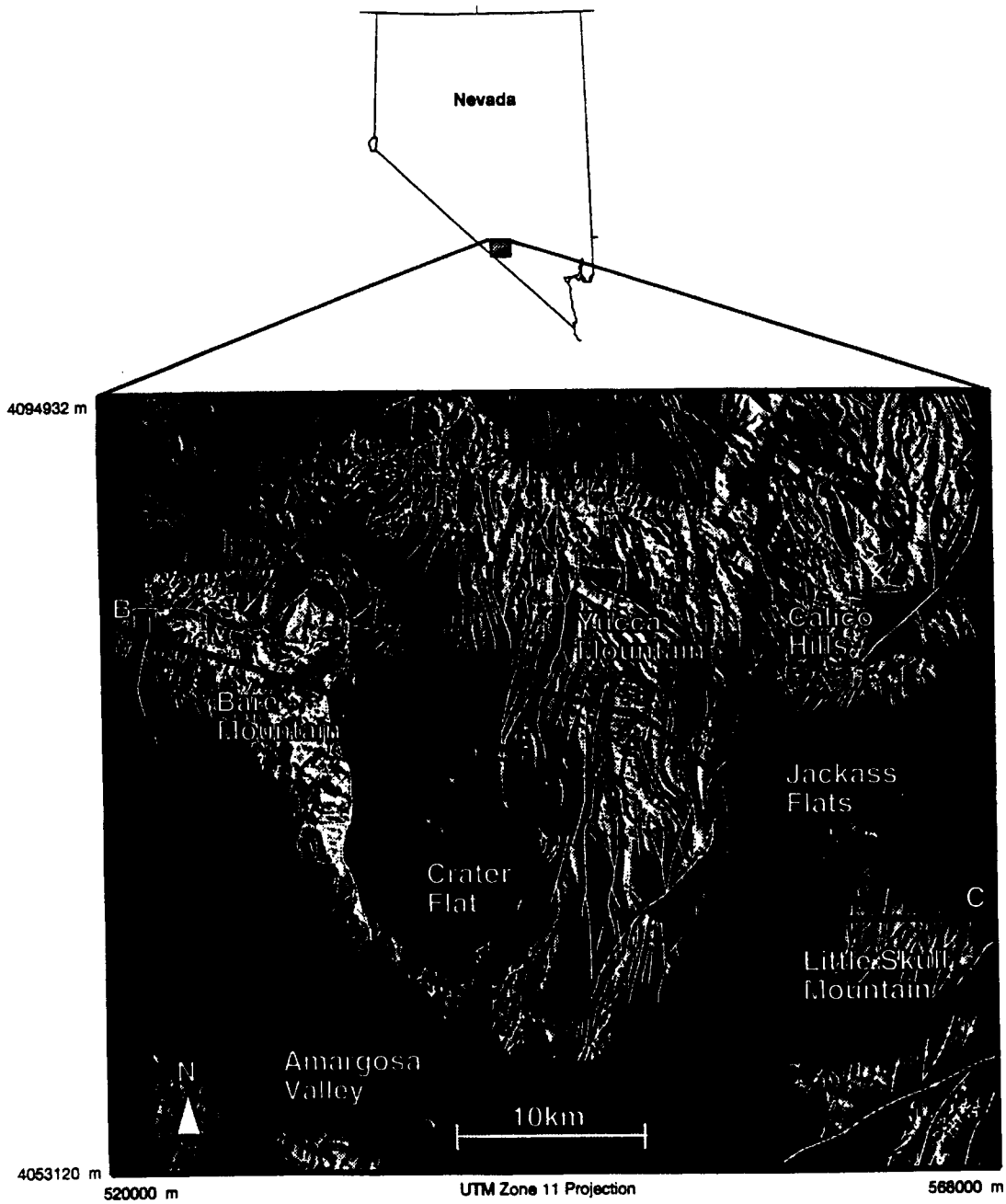
Nevada
4094932 m
B
Bare Mountain
Yucca Mountain
Calico Hills
Jackass Flats
Crater Flat
C
Little Skull Mountain
Amargosa Valley
N
10km
4053120 m
520000 m
UTM Zone 11 Projection
568000 m

Fig 1

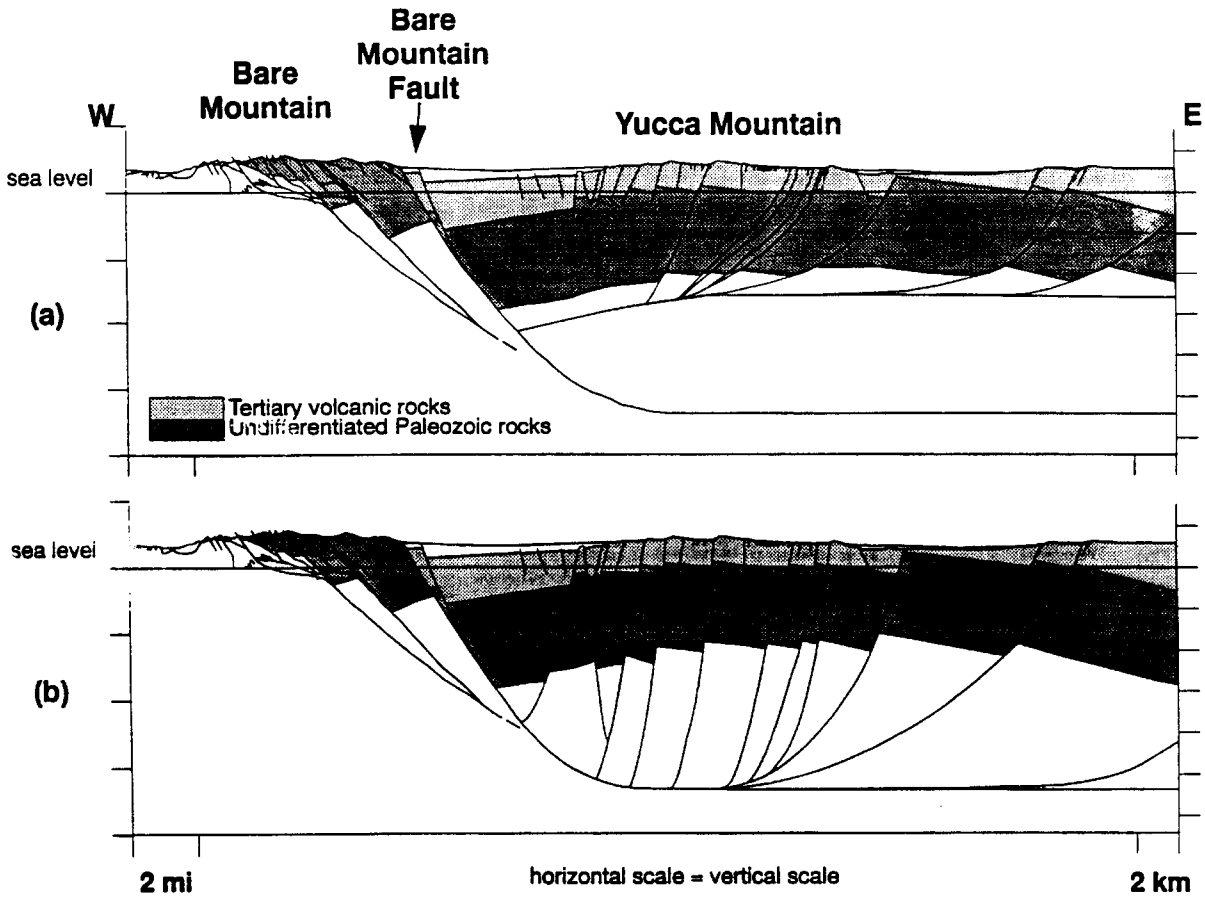
Bare Mountain Fault
Bare Mountain
W
Yucca Mountain
E
sea level
(a)
Tertiary volcanic rocks
Undifferentiated Paleozoic rocks
sea level
(b)
2 mi
horizontal scale = vertical scale
2 km

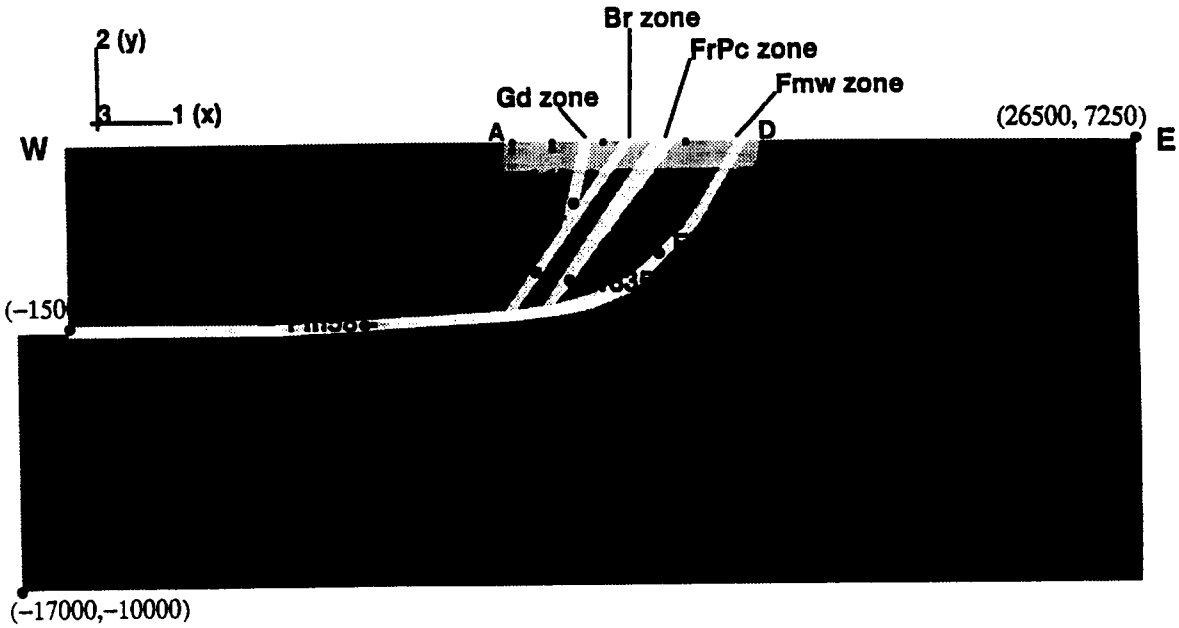
2 (y)
3
1 (x)
W
Br zone
FrPc zone
Fmw zone
Gd zone
A
D
(26500, 7250)
E
(−150
(−17000,−10000)

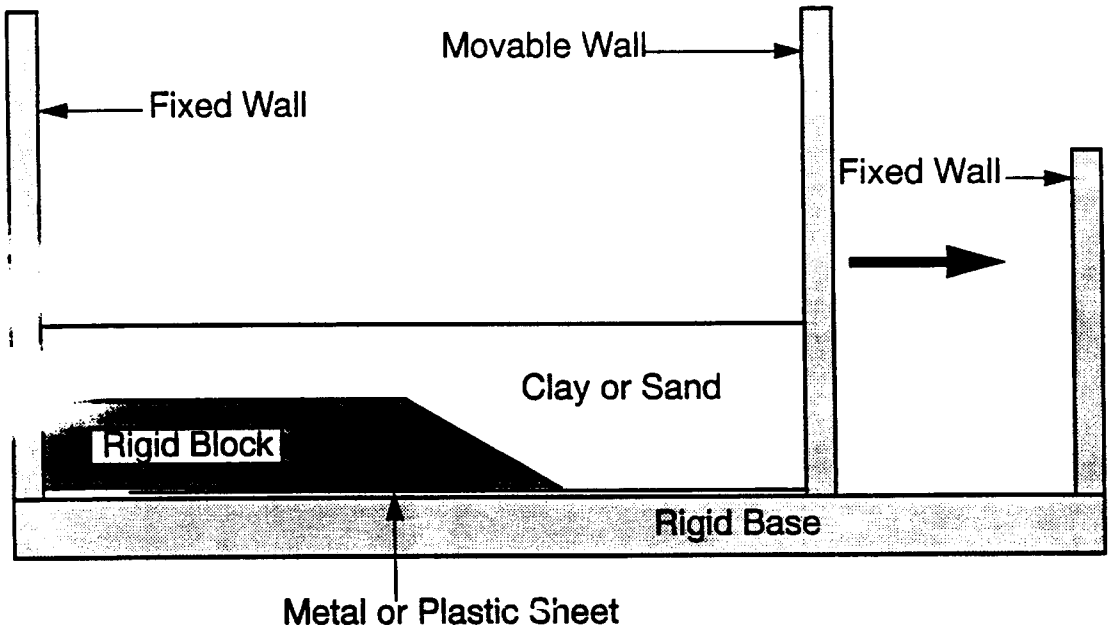
Movable Wall
Fixed Wall
Fixed Wall
Clay or Sand
Rigid Block
Rigid Base
Metal or Plastic Sheet

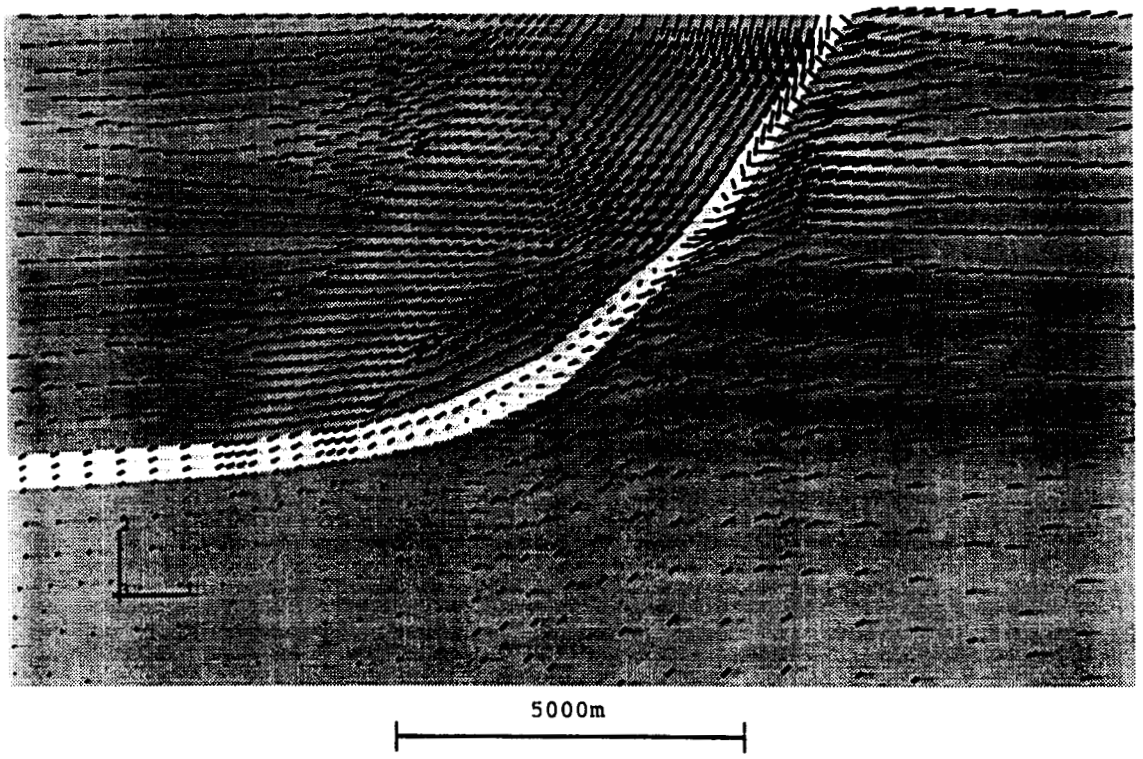
5000m

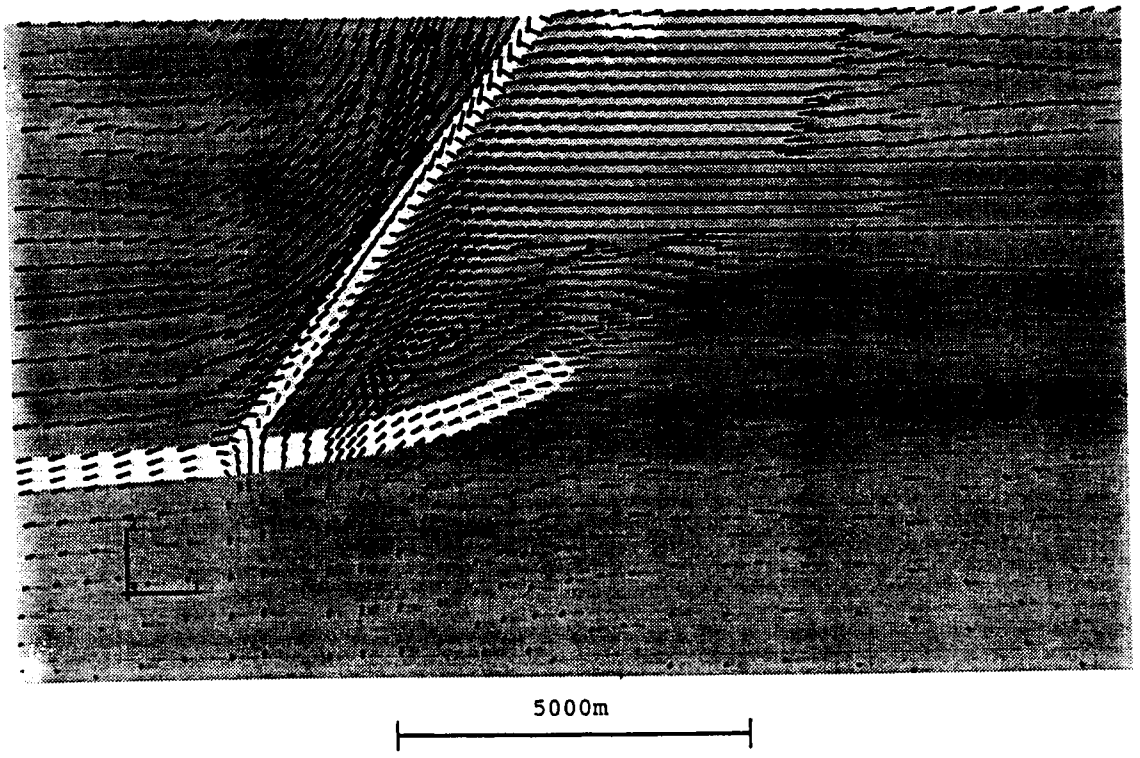
5000m

59/10

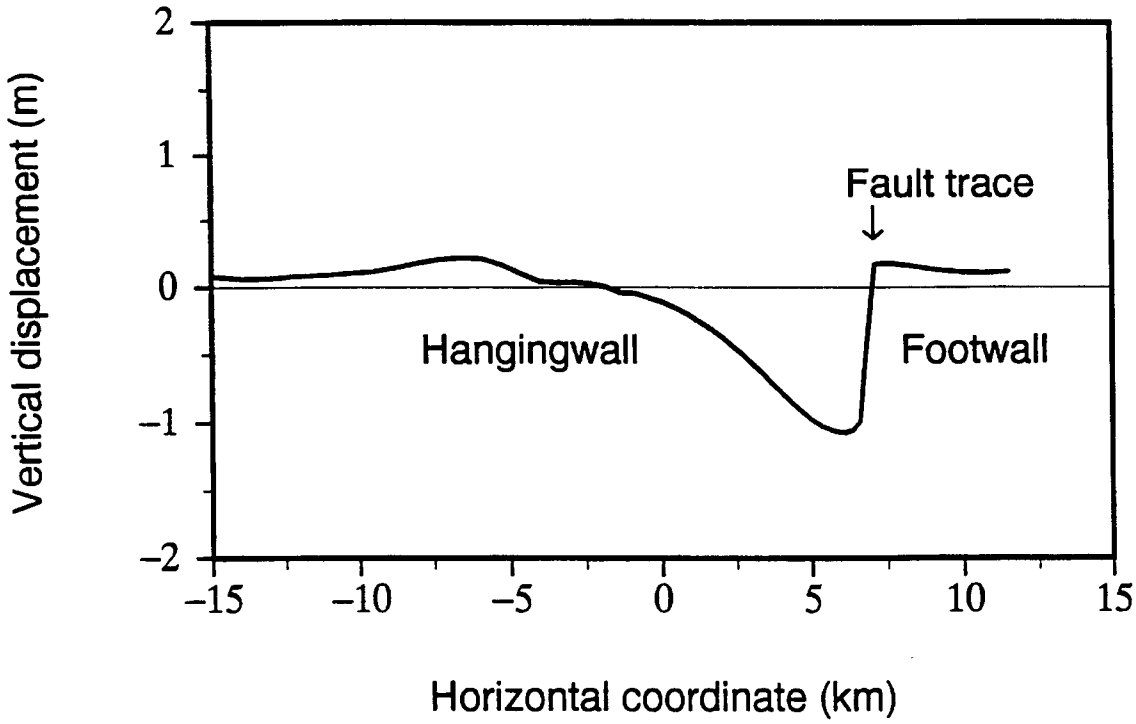
Vertical displacement (m)
2
1
0
−1
−2
Fault trace
Hangingwall
Footwall
−15
−10
−5
0
5
10
15
Horizontal coordinate (km)

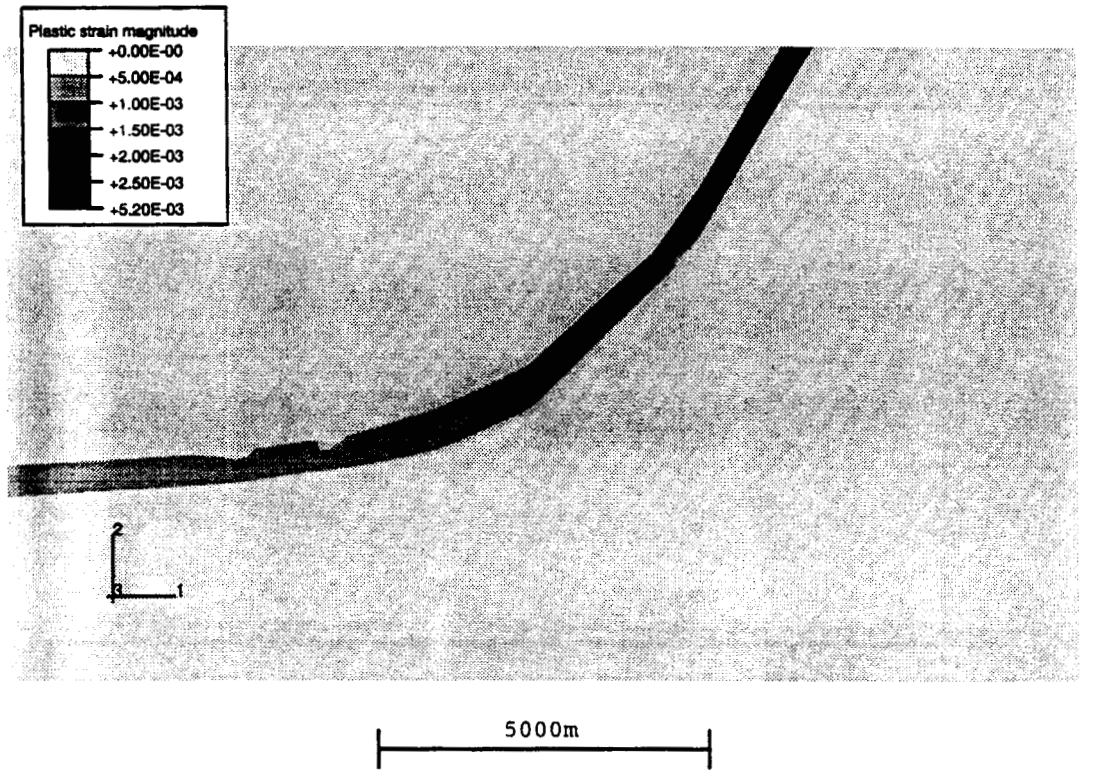
Plastic strain magnitude
+0.00E-00
+5.00E-04
+1.00E-03
+1.50E-03
+2.00E-03
+2.50E-03
+5.20E-03
2
3
1
5000m

61/70

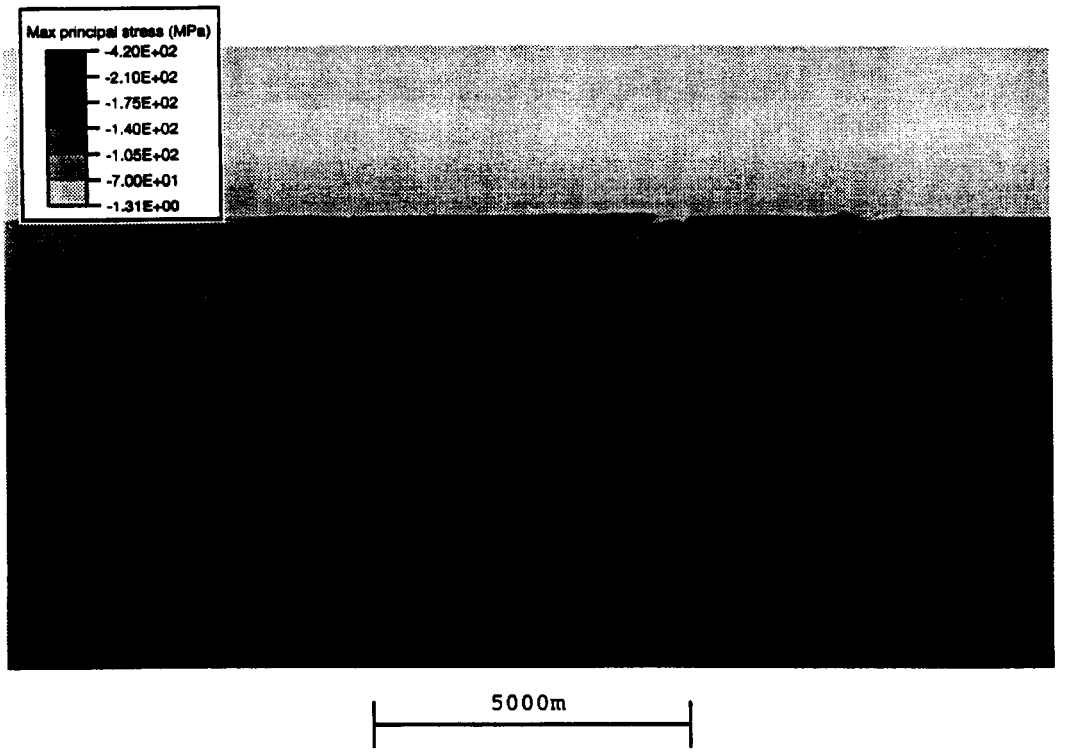
Max principal stress (MPa)
-4.20E+02
-2.10E+02
-1.75E+02
-1.40E+02
-1.05E+02
-7.00E+01
-1.31E+00
5000m

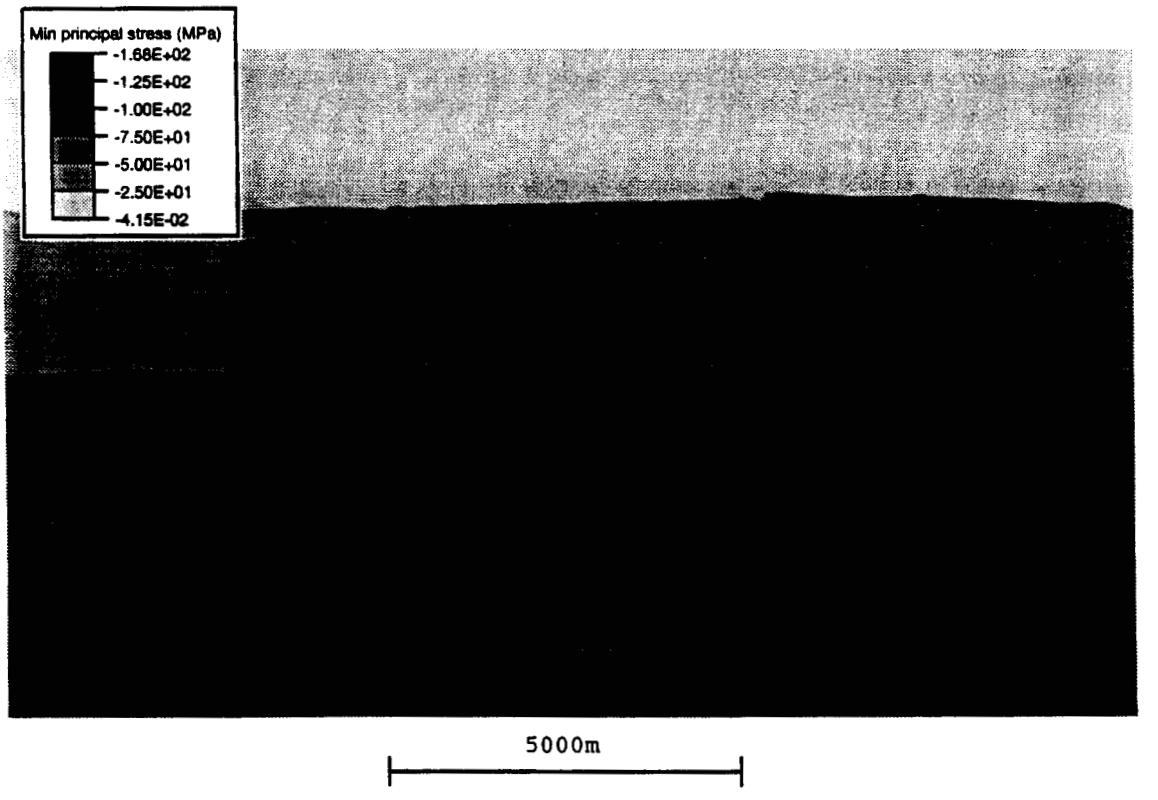
Min principal stress (MPa)
-1.68E+02
-1.25E+02
-1.00E+02
-7.50E+01
-5.00E+01
-2.50E+01
-4.15E-02
5000m

63/10

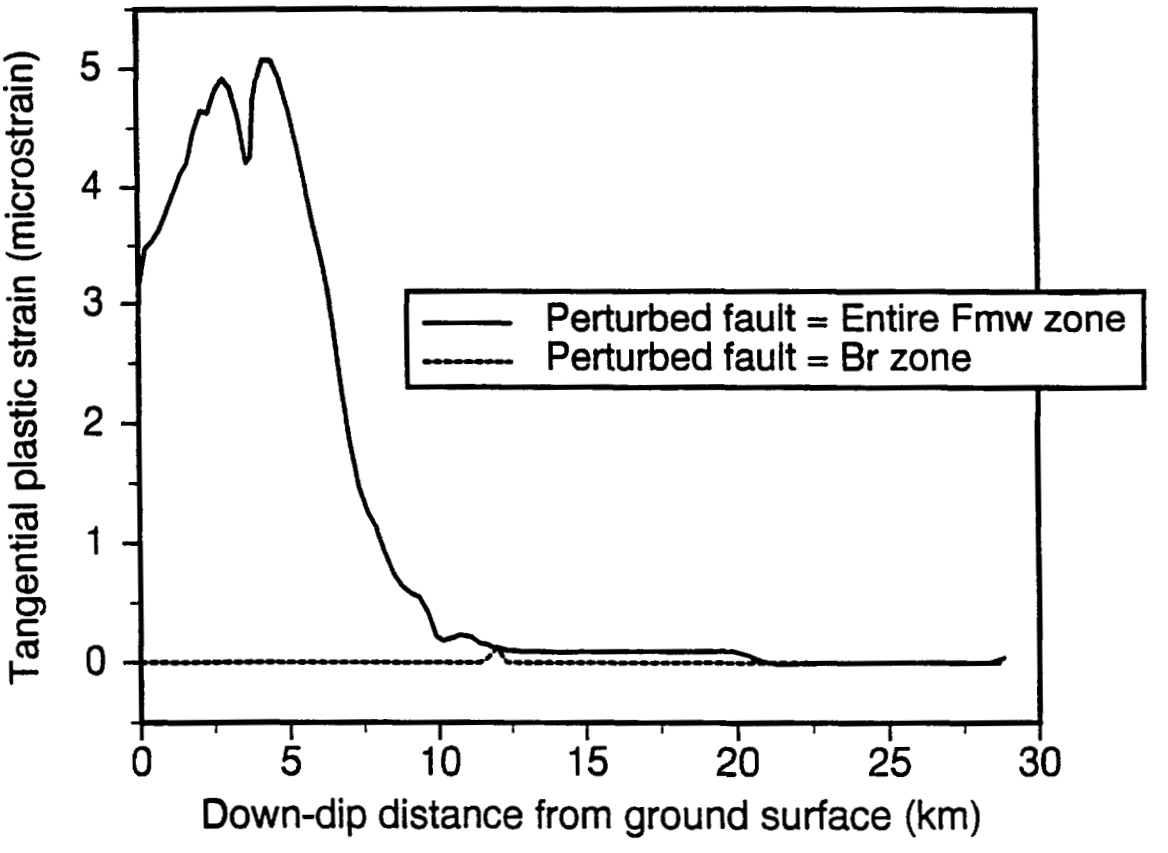
Tangential plastic strain (microstrain)
5
4
3
2
1
0
0
5
10
15
20
25
30
Down-dip distance from ground surface (km)
Perturbed fault = Entire Fmw zone
Perturbed fault = Br zone

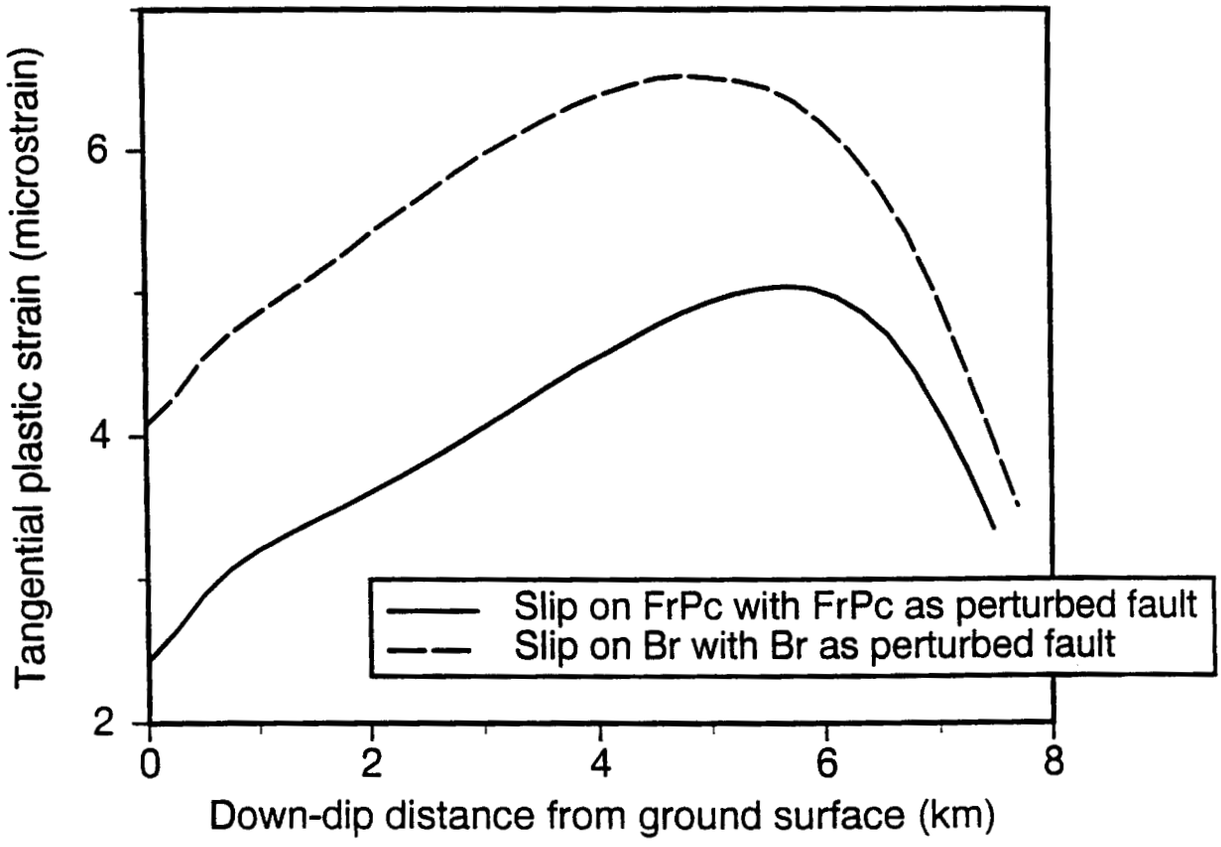
Tangential plastic strain (microstrain)
6
4
2
0
2
4
6
8
Down-dip distance from ground surface (km)
Slip on FrPc with FrPc as perturbed fault
Slip on Br with Br as perturbed fault

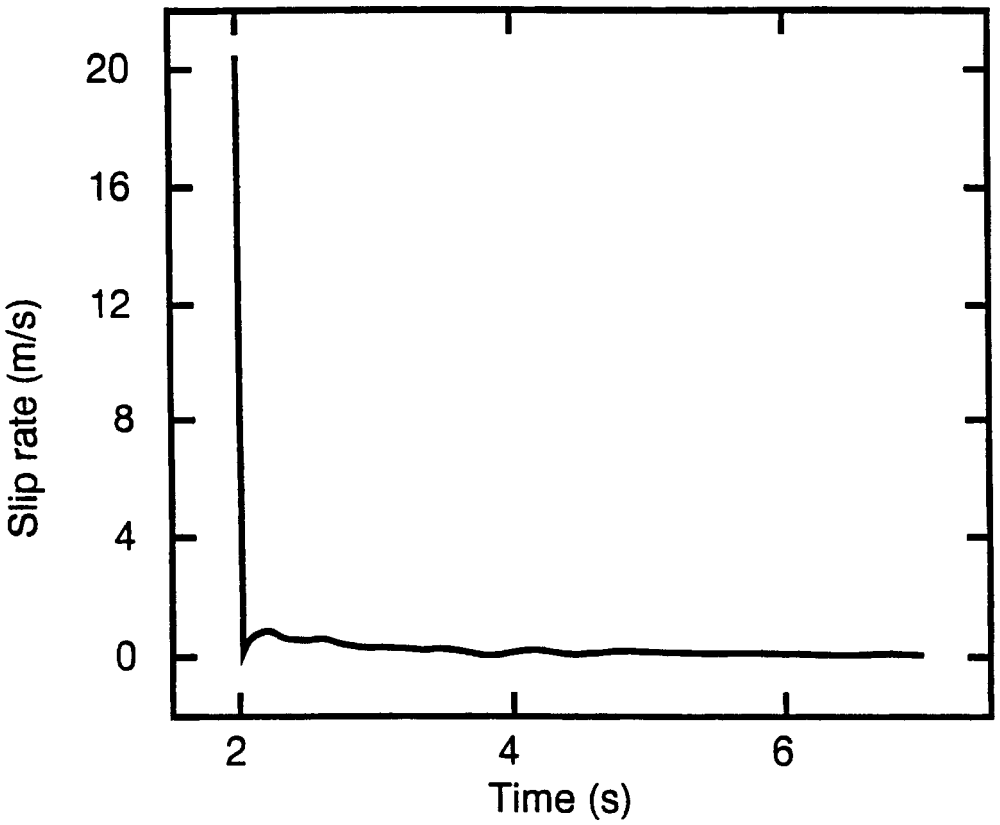

Fig 13

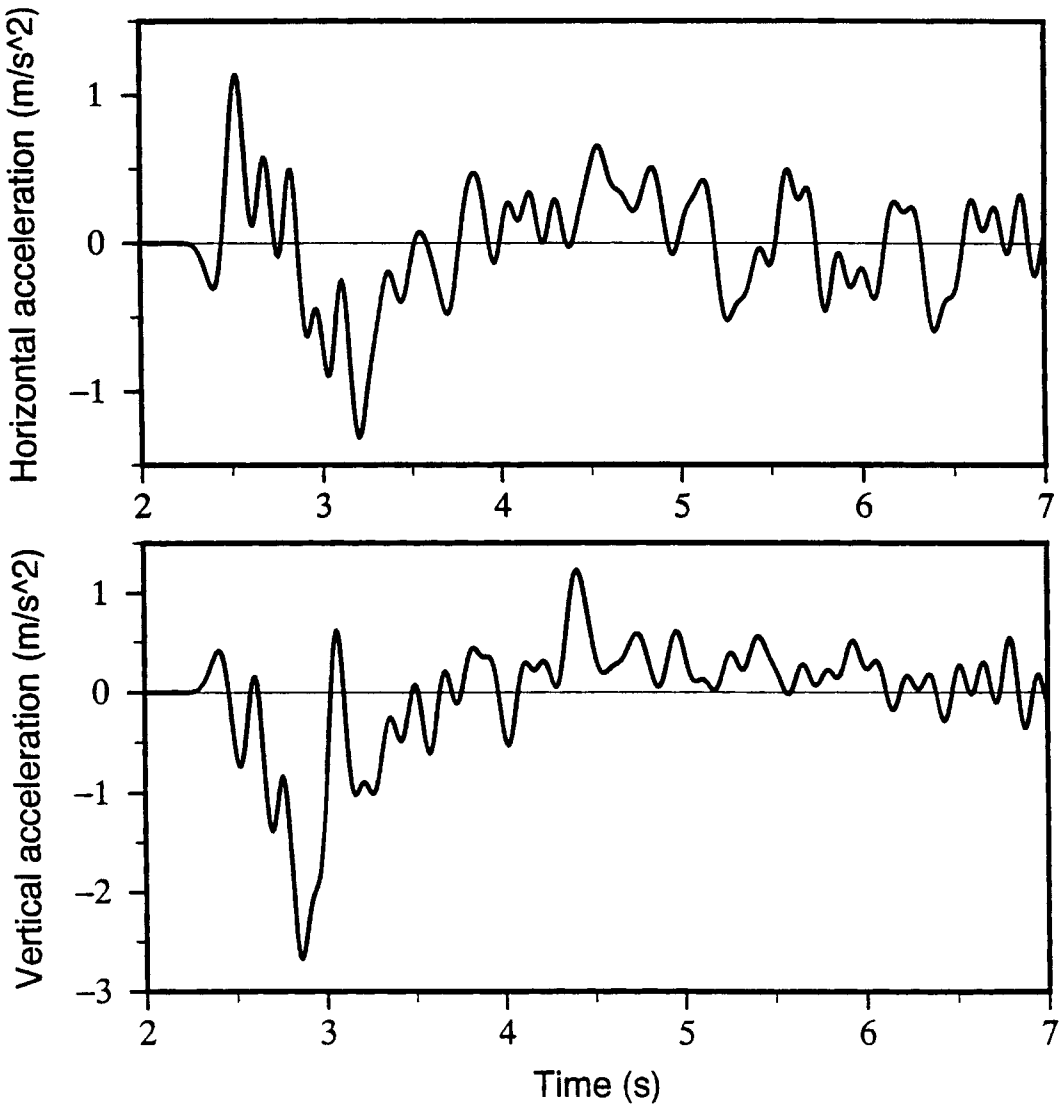
Horizontal acceleration (m/s^2)
1
0
−1
2
3
4
5
6
7
Vertical acceleration (m/s^2)
1
0
−1
−2
−3
2
3
4
5
6
7
Time (s)

Fig. 4

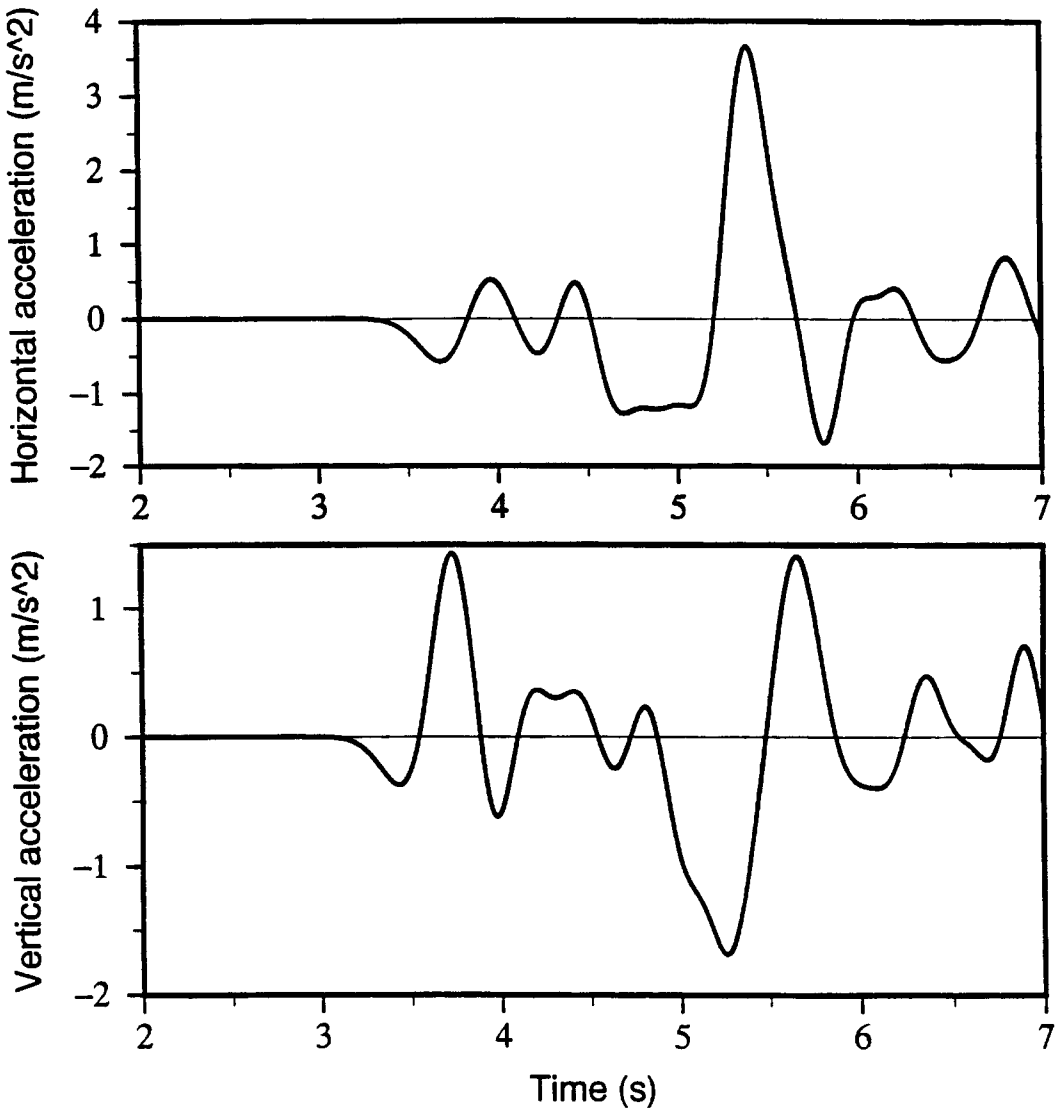
Horizontal acceleration (m/s^2)
4
3
2
1
0
−1
−2
2
3
4
5
6
7
Vertical acceleration (m/s^2)
1
0
−1
−2
2
3
4
5
6
7
Time (s)

Fig 15

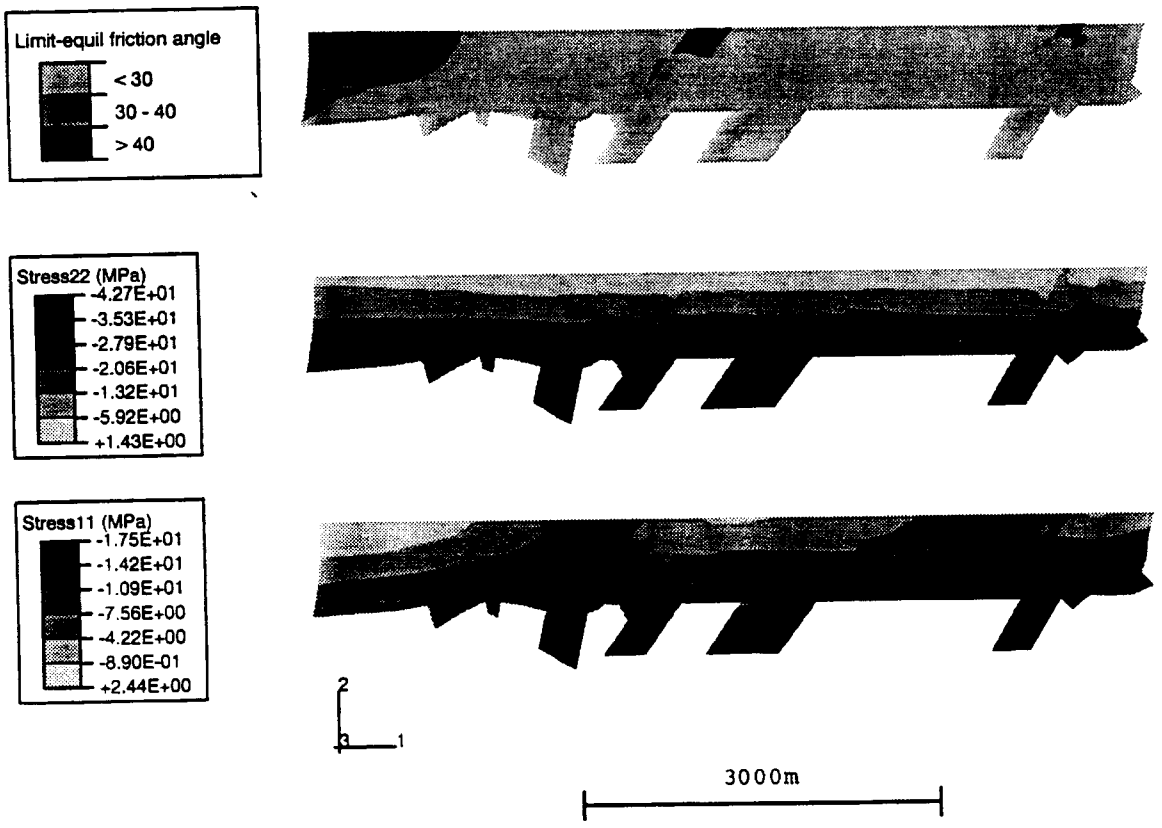
Limit-equil friction angle
< 30
30 - 40
> 40
Stress22 (MPa)
-4.27E+01
-3.53E+01
-2.79E+01
-2.06E+01
-1.32E+01
-5.92E+00
+1.43E+00
Stress11 (MPa)
-1.75E+01
-1.42E+01
-1.09E+01
-7.56E+00
-4.22E+00
-8.90E-01
+2.44E+00
2
3
1
3000m

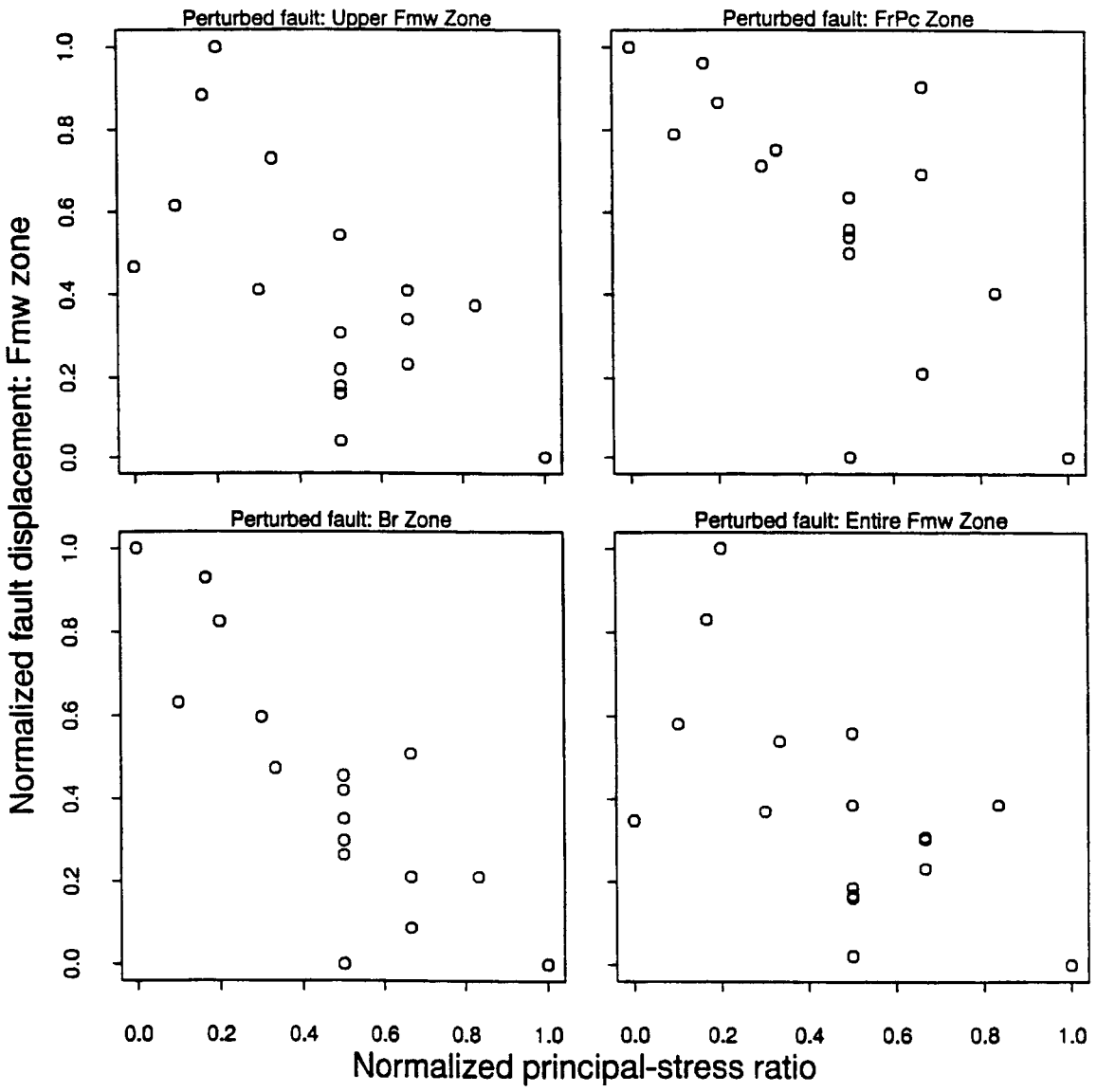
Perturbed fault: Upper Fmw Zone
Perturbed fault: FrPc Zone
Perturbed fault: Br Zone
Perturbed fault: Entire Fmw Zone
Normalized fault displacement: Fmw zone
Normalized principal-stress ratio
0.0
0.2
0.4
0.6
0.8
1.0

Fig 17

10/10

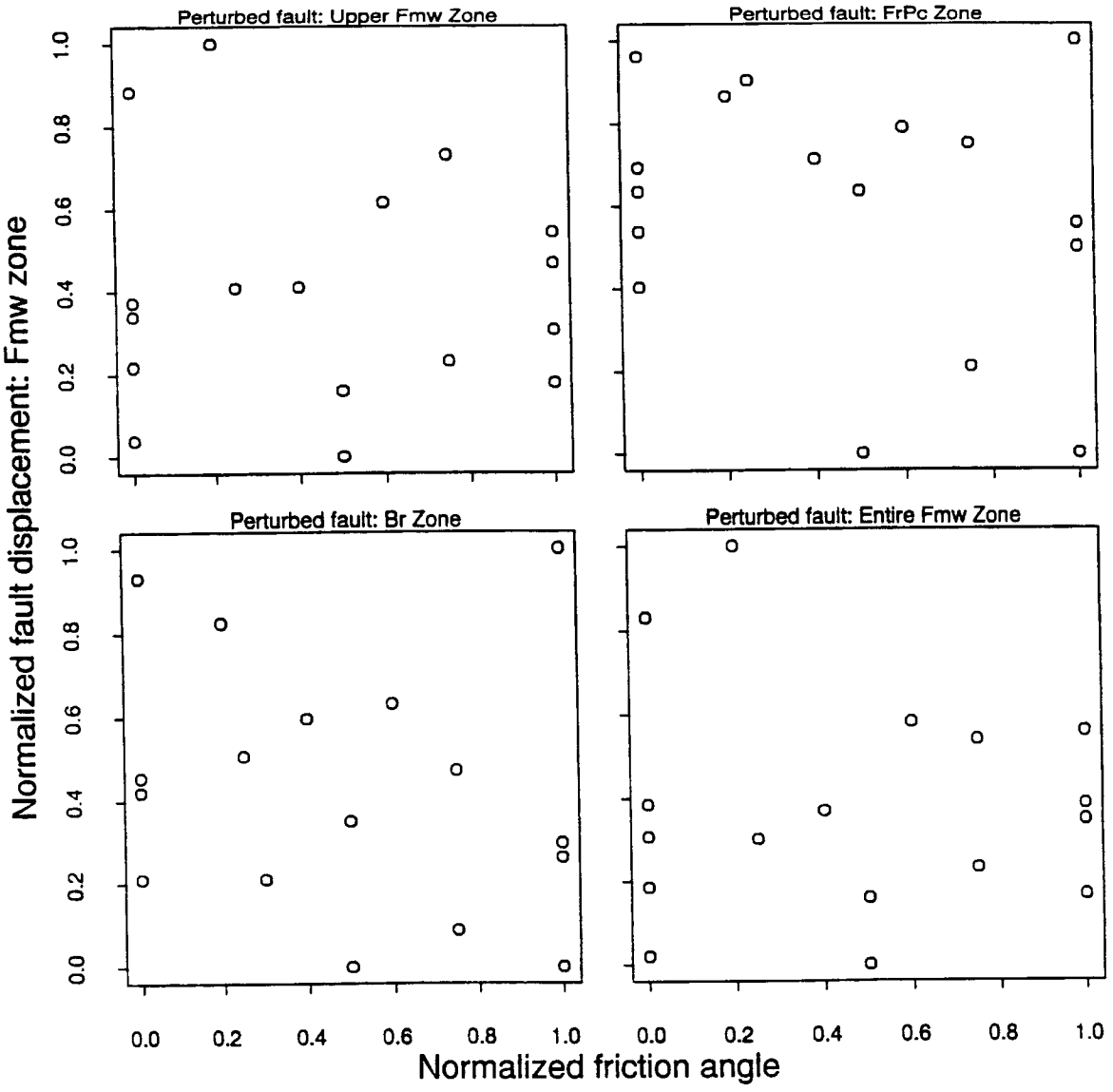
Perturbed fault: Upper Fmw Zone
Perturbed fault: FrPc Zone
Perturbed fault: Br Zone
Perturbed fault: Entire Fmw Zone
Normalized fault displacement: Fmw zone
Normalized friction angle
0.0
0.2
0.4
0.6
0.8
1.0

Fig 15